The Astrophysical Journal Supplement Series, 277:26 (23pp), 2025 March https://doi.org/10.3847/1538-4365/adaf27

The S-PLUS Ultra-short Survey: Photometric Recalibration with the Best Star Database

Xiaolu Li[1,2], Kai Xiao[3,4], Yang Huang[3,5], Haibo Yuan[4,6], Yanke Tang[1,2], Timothy C. Beers[7], Bowen Huang[4,6], Mingyang Ma[4,6], Pedro K. Humire[8], Alvaro Alvarez-Candal[9], Federico Sestito[10], Ning Gai[1,2], Yongna Mao[5], Hongrui Gu[3,5], Zhenzhao Tao[11,12], Lin Yang[13], Shuai Xu[4,6], and Rong Hu[14]

[1] College of Physics and Electronic Information, Dezhou University, Dezhou 253023, People's Republic of China; tyk@dzu.edu.cn
[2] International Centre of Supernovae, Yunnan Key Laboratory, Kunming 650216, People's Republic of China
[3] School of Astronomy and Space Science, University of Chinese Academy of Sciences, Beijing 100049, People's Republic of China; xiaokai@ucas.ac.cn, huangyang@ucas.ac.cn
[4] Institute for Frontiers in Astronomy and Astrophysics, Beijing Normal University, Beijing 102206, People's Republic of China; yuanhb@bnu.edu.cn
[5] CAS Key Lab of Optical Astronomy, National Astronomical Observatories, Chinese Academy of Sciences, Beijing 100012, People's Republic of China
[6] School of Physics and Astronomy, Beijing Normal University, No. 19, Xinjiekouwai St., Haidian District, Beijing 100875, People's Republic of China
[7] Department of Physics and Astronomy and JINA Center for the Evolution of the Elements (JINA-CEE), University of Notre Dame, Notre Dame, IN 46556, USA
[8] Departamento de Astronomia, Instituto de Astronomia, Geofísica e Ciências Atmosféricas da USP, Cidade Universitária, 05508-900 São Paulo, SP, Brazil
[9] Instituto de Astrofísica de Andalucía, CSIC, Apt. 3004, 18080 Granada, Spain
[10] Centre for Astrophysics Research, Department of Physics, Astronomy and Mathematics, University of Hertfordshire, Hatfield, AL10 9AB, UK
[11] College of Computer and Information, Dezhou University, Dezhou 253023, People's Republic of China
[12] Institute for Astronomical Science, Dezhou University, Dezhou 253023, People's Republic of China
[13] Department of Cyber Security, Beijing Electronic Science and Technology Institute, Beijing 100070, People's Republic of China
[14] Department of Physics, Beijing Technology and Business University, Beijing 100048, People's Republic of China
Received 2024 November 1; revised 2024 December 19; accepted 2025 January 6; published 2025 March 3

Abstract

We present an independent validation and comprehensive recalibration of S-PLUS Ultra-short Survey (USS) DR1 12-band photometry using about 30,000–70,000 standard stars from the Best Star (BEST) database. We identify the spatial variation of zero-point offsets, up to 30–40 mmag for blue filters (*u*, *J*0378, and *J*0395) and 10 mmag for others, predominantly due to the higher uncertainties of the technique employed in the original USS calibration. Moreover, we detect large- and medium-scale CCD position-dependent systematic errors, up to 50 mmag, primarily caused by different aperture and flat-field corrections. We then recalibrate the USS DR1 photometry by correcting the systematic shifts for each tile using second-order two-dimensional polynomial fitting combined with a numerical stellar flat-field correction method. The recalibrated results from the XP spectrum based synthetic photometry and the stellar color regression standards are consistent within 6 mmag in the USS zero-points, demonstrating both the typical precision of the recalibrated USS photometry and a sixfold improvement in USS zero-point precision. Further validation using the Sloan Digital Sky Survey and Pan-STARRS1, as well as LAMOST DR10 and Gaia photometry, also confirms this precision for the recalibrated USS photometry. Our results clearly demonstrate the capability and efficiency of the BEST database in improving calibration precision to the millimagnitude level for wide-field photometric surveys. The recalibrated USS DR1 photometry is publicly available on ChinaVO at doi:10.12149/101503.

Unified Astronomy Thesaurus concepts: Stellar photometry (1620); Astronomy data analysis (1858); Calibration (2179)

1. Introduction

The current era of astronomy is characterized by the flourishing of wide-field photometric survey projects, with a continuous influx of photometric data significantly impacting various fields within the discipline. Ensuring the consistency of flux measurements between widely separated targets under varying observing conditions, across different detector positions, and at different observing times is crucial for the success of these projects. Achieving high-precision photometric calibration is essential to conduct high-precision scientific research because the precision of photometric calibration limits the detection accuracy in astronomical measurements.

Achieving millimagnitude-level photometric calibration in ground-based photometric surveys presents a significant challenge, due to the complexity of accounting for systematic errors introduced by instrumental effects and the Earth's atmospheric influence (C. W. Stubbs & J. L. Tonry 2006). Historically, the limited number and precision of photometric standard stars have made it difficult to accurately measure and correct these errors. However, the recent release of extensive stellar atmospheric parameters from large-scale spectroscopic surveys such as LAMOST (X.-Q. Cui et al. 2012; L.-C. Deng et al. 2012; G. Zhao et al. 2012; X.-W. Liu et al. 2014), along with Gaia photometry and BP/RP spectra (BP and RP are the abbreviations for Blue Photometer and Red Photometer, respectively; BP/RP is often shortened as XP; Gaia Collaboration et al. 2023b), offers an opportunity to establish a large array of high-precision photometric standard stars. This advancement enables more accurate measurement and correction of the complex systematic errors.

In recent years, a series of photometric calibration methods have been proposed (B. Huang & H. Yuan 2022; B. Huang et al. 2022), including both "hardware/observation-driven" and "software/physics-driven" methods. Among them, the stellar color regression (SCR) method and the Gaia XP spectrum based synthetic photometry (XPSP) method have achieved outstanding results. The SCR method, first proposed by H. Yuan et al. (2015), predicts the intrinsic colors of stars using a few physical quantities. For example, the stellar atmospheric parameters can be used to predict the intrinsic colors. Applied to Sloan Digital Sky Survey (SDSS; D. G. York et al. 2000) Stripe 82 (Ž. Ivezić et al. 2007), the SCR method achieved a threefold improvement in color and magnitude accuracy, with precision levels of 2–5 mmag (H. Yuan et al. 2015; B. Huang & H. Yuan 2022). Application of this method to Gaia Data Release 2 (Gaia Collaboration et al. 2018) and Early Data Release 3 (EDR3; Gaia Collaboration et al. 2021a, 2021b) resulted in the correction of systematic errors to a precision of 1 mmag (Z. Niu et al. 2021a, 2021b; L. Yang et al. 2021). The SCR method was also used to recalibrate the SkyMapper Southern Survey (C. Wolf et al. 2018) Data Release 2, identifying significant zero-point offsets in the *u* and *v* bands (Y. Huang et al. 2021). Furthermore, the method corrected spatially dependent and magnitude-dependent systematic errors in Pan-STARRS1 (PS1; J. L. Tonry et al. 2012) Data Release 1, achieving 1–2 mmag precision at a spatial resolution of 14″ (K. Xiao & H. Yuan 2022; K. Xiao et al. 2023b), and was also applied to Stellar Abundance and Galactic Evolution Survey (SAGES; J. Zheng et al. 2018, 2019; Z. Fan et al. 2023) photometry, achieving precisions of 1–2 mmag for the *gri* bands (K. Xiao et al. 2023a) and ⩽5 mmag for the *uv* bands.

In 2022 June, Gaia DR3 released XP spectra for approximately 220 million sources (J. M. Carrasco et al. 2021; Gaia Collaboration et al. 2023b), mostly with magnitudes $G < 17.65$ and wavelengths from 336 to 1020 nm, which were calibrated both internally (J. M. Carrasco et al. 2021; F. De Angeli et al. 2023) and externally (P. Montegriffo et al. 2023). Based on the Gaia XP spectra, Gaia Collaboration et al. (2023a) proposed the XPSP method. However, Gaia XP spectra exhibit systematic errors related to magnitude, color, and extinction, particularly below 400 nm (P. Montegriffo et al. 2023; B. Huang et al. 2024). Recently, B. Huang et al. (2024) performed comprehensive corrections on the Gaia XP spectra. The corrected Gaia XP spectra were used to improve the XPSP method (K. Xiao et al. 2023c), which no longer relies on 343 spectral coefficients and can directly derive multiband magnitudes from the corrected spectra. This method achieves higher accuracy in constructing photometric standard stars. The improved XPSP method was applied to the photometric recalibration of J-PLUS DR3 data (C. López-Sanjuan et al. 2024), achieving zero-point precision of 1–5 mmag—a twofold improvement (K. Xiao et al. 2023c).

More recently, using the SCR and improved XPSP methods, K. Xiao et al. (2025, in preparation) created the Best Star (BEST) database, which includes over 200 million high-precision photometric standard stars.[15] This database covers more than 10 photometric systems, such as the Gaia (Gaia Collaboration et al. 2021a, 2021b), Landolt (J. L. Clem & A. U. Landolt 2013, 2016), J-PLUS (A. J. Cenarro et al. 2019), S-PLUS (C. Mendes de Oliveira et al. 2019), J-PAS (N. Benitez et al. 2014), SDSS (D. G. York et al. 2000), PS1 (J. L. Tonry et al. 2012), CSST (H. Zhan 2018), LSST (Ž. Ivezić et al. 2019), SkyMapper (C. Wolf et al. 2018), and SiTian project (J. Liu et al. 2021) systems, and spans hundreds of bands, providing coverage for stars brighter than 17.65 mag across the entire sky. In the process, we first predicted the XPSP standard magnitudes across those photometric systems based on the corrected Gaia XP spectra by B. Huang et al. (2024) and the total transmission function of each photometric band using an improved XPSP method. For bands slightly beyond the wavelength coverage of the Gaia XP spectra, such as the SDSS *u* band, we used a linear fit to extrapolate the spectra, following the approach described by K. Xiao et al. (2023c). Following that, using the extensive stellar atmospheric parameters provided by LAMOST (X.-Q. Cui et al. 2012; L.-C. Deng et al. 2012; G. Zhao et al. 2012; X.-W. Liu et al. 2014), GALAH (G. M. De Silva et al. 2015), and others, as well as the XPSP magnitudes, we employed the SCR method to derive the SCR standard magnitudes for stars with known stellar atmospheric parameters. There is good consistency between the SCR and the XPSP standard photometry, as noted by K. Xiao et al. (2025, in preparation). Below we present a detailed comparison of the consistency between the standard stars constructed using these two methods across the S-PLUS Ultra-short Survey (USS) photometric filters.

As a subsurvey of the S-PLUS survey, the USS employs a 12-filter system (H. D. Perottoni et al. 2024), comprising seven narrowband/medium-band filters and five broadband filters. This imaging survey spans the same sky area as the overall S-PLUS Main Survey, but with significantly shorter exposure times of 3–20 s (one-fortieth to one-thirty-third of those of the S-PLUS Main Survey). The primary goal of the USS is to uncover bright, extremely metal-poor ($-4.0 \leqslant [Fe/H] < -3.0$) and ultra-metal-poor ($[Fe/H] < -4.0$) stars. As K. Xiao et al. (2024a) highlighted, the accuracy of photometric data and the sensitivity of the photometric bands are both crucial in photometry-based stellar metallicity measurement. To achieve this objective, high-precision photometric calibration of the USS DR1 data is essential.

In this study, we perform a photometric recalibration of the USS DR1 data aiming to achieve uniform photometry with an accuracy at the millimagnitude level using the BEST database. The structure of this paper is as follows. We present the data set used in this work in Section 2. In Section 3, we provide a detailed description of the independent calibration validation of the USS DR1 data, followed by the correction of systematic errors in Section 4. Section 5 addresses the zero-point precision of the photometric recalibration. A discussion is presented in Section 6, followed by a summary and conclusions provided in Section 7.

2. Data

2.1. USS DR1

USS DR1 includes 163 tiles along the celestial equator for all bands, with saturation magnitudes of about 10th magnitude (in the broadband SDSS-like filters), and with each tile measuring 2 deg^2 (H. D. Perottoni et al. 2024). It is important to note that the USS continues observing even when not all observations are conducted under optimal photometric conditions, such as when cirrus clouds are present. As detailed in H. D. Perottoni et al. (2024), the USS provides aperture instrumental photometry obtained using SExtractor (E. Bertin & S. Arnouts 1996). Aperture corrections were performed based on the 3″ aperture magnitudes by measuring the magnitudes in 32 concentric apertures centered around each point source, averaging the magnitude changes in larger apertures until convergence, considering sources with signal-to-noise ratios (SNRs) between 30 and 1000. The result of the aperture correction is constant for each tile, as shown in Figure A1. For photometric calibration, H. D. Perottoni et al. (2024) first used stellar spectral energy distribution (SED)

[15] Here, the photometric standard stars are a series of stars whose uniformity and accuracy of magnitude have been meticulously ensured across the 12 passbands of the S-PLUS photometric system.

fitting to convert PS1 standard stars from the ATLAS all-sky stellar reference catalog (ATLAS Refcat2; J. L. Tonry et al. 2018) to the USS system for the *g*-, *J*0515-, *r*-, *J*0660-, *i*-, *J*0861-, and *z*-band photometry, then used the stellar locus (SL; F. Almeida-Fernandes et al. 2022) method to calibrate the *u*, *J*0378, *J*0395, *J*0410, and *J*0430 bands based on the calibrated *g* and *i* magnitudes (e.g., $u - g$ versus $g - i$), and finally performed SED-based calibration for all 12 bands.

The final catalog of USS DR1 includes photometrically calibrated magnitudes measured in 3″ (labeled `APER_3`) and 6″ (`APER_6`) diameter apertures, aperture-corrected `APER_3` magnitudes (`PStotal`), and stellar profile information, such as the normalized full width at half-maximum (FWHM; labeled `FWHM_n`) and ellipticity (`ELLIPTICITY`). All USS DR1 data is publicly available through the splus.cloud service.[16] The USS magnitudes mentioned in this paper refer to the `PStotal` magnitudes.

We stress that, if the assumption that a 3″ aperture is the best aperture is flawed, the aperture correction of USS DR1 may be suboptimal. Moreover, systematic errors from external reference catalogs (e.g., ATLAS Refcat2) might propagate into the USS data, and the SL method's different treatment of stellar metallicity may introduce metallicity-dependent systematics in the blue filters. Additionally, the spatial inhomogeneity of image quality and astrometric centering, as well as a different flat-field correction, could cause CCD position-dependent systematic errors in USS DR1.

2.2. BEST Standards in the USS System

The BEST database (K. Xiao et al. 2025, in preparation) provides (1) a 12-band standard star catalog in the USS system, encompassing approximately five million SCR standard stars predicted using the SCR method based on spectroscopic data from LAMOST (X.-Q. Cui et al. 2012; L.-C. Deng et al. 2012; G. Zhao et al. 2012; X.-W. Liu et al. 2014) DR10[17] and corrected Gaia EDR3 photometric data (L. Yang et al. 2021), and (2) over 200 million XPSP standard stars derived using an improved XPSP method (K. Xiao et al. 2023c) based on "corrected" Gaia XP spectra (B. Huang et al. 2024). For reddening correction in the SCR method, we avoid using the dust-reddening map by D. J. Schlegel et al. (1998), as it has proven to be unreliable at low Galactic latitudes, and exhibits spatially dependent systematic errors (Y. Sun et al. 2022). Instead, we employ the star pair method (H. B. Yuan et al. 2013; R. Zhang & H. Yuan 2020) to determine the values of $E(G_{\rm BP} - G_{\rm RP})$.

The XPSP standard stars are distributed across the entire sky, with magnitudes ranging from about 10 to 17.65 mag. The SCR standard stars are main-sequence stars ($\log g > -3.4 \times 10^{-4} \times T_{\rm eff} + 5.8$) confined to the sky region north of decl. $-10°$, and they comply with the following constraints: $4500 \leqslant T_{\rm eff} \leqslant 6500$ K and $[{\rm Fe/H}] \geqslant -1$ for robust fitting in the SCR method, `phot_bp_rp_excess_factor` $< 1.3 + 0.06 \times (G_{\rm BP} - G_{\rm RP})^2$ to avoid poor Gaia $G_{\rm BP}/G_{\rm RP}$ photometry, and an SNR for the LAMOST *g*-band spectra greater than 20.

To evaluate the consistency between the magnitudes of the SCR and the XPSP standard stars, Figure 1 presents their difference as functions of the Gaia *G* magnitude, Gaia color $G_{\rm BP} - G_{\rm RP}$, and extinction $E(G_{\rm BP} - G_{\rm RP})$. Due to the low

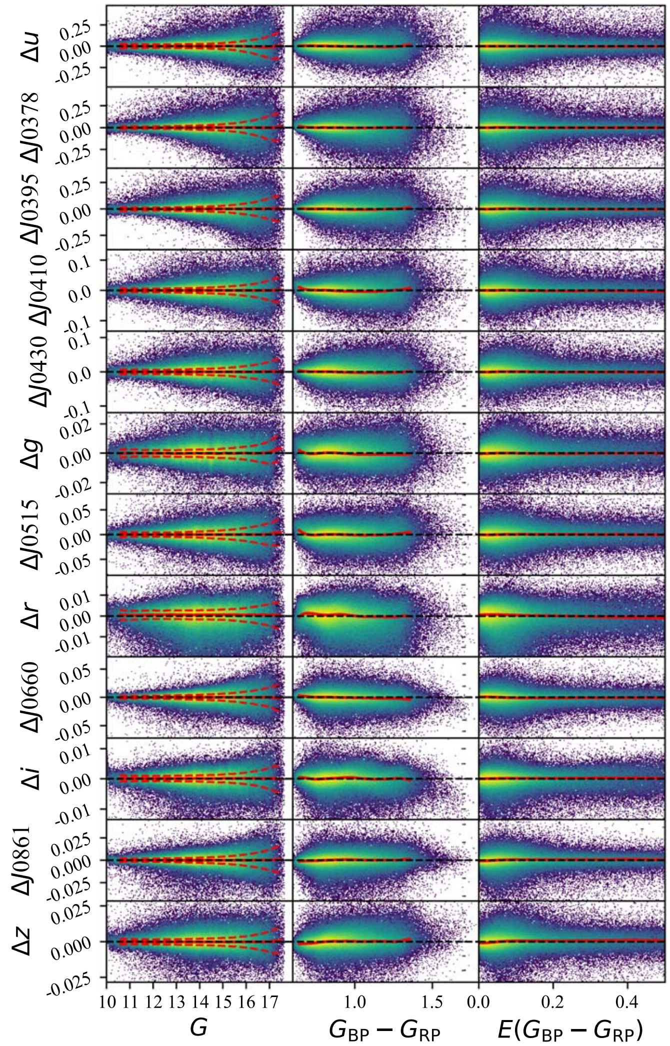

Figure 1. Magnitude offsets between the XPSP and the SCR standard stars, as functions of Gaia G, $G_{\rm BP} - G_{\rm RP}$, and $E(G_{\rm BP} - G_{\rm RP})$, for all 12 bands. The colors represent the density of points. For each panel, the zero residuals and median values of the magnitude offsets are denoted by black dashed lines and red curves, respectively. The red dashed curves in the leftmost panels represent the standard deviations of the points, estimated using Gaussian fitting with a running width of 0.5 mag and a running step of 0.2 mag.

extinction ($E(B - V) \leqslant 0.068$ mag; H. D. Perottoni et al. 2024) of stars in USS DR1, only stars with extinction $E(G_{\rm BP} - G_{\rm RP}) \leqslant 0.5$ are considered here. As expected, no dependence on magnitude, color, or extinction is found. At the bright end, the standard deviation is smallest, but as the stellar brightness decreases, the standard deviation first increases slowly and then rapidly. For example, in the *i* band, the scatter is only 0.9 mmag for $G \sim 11$, increases slightly to 1.3 mmag at $G = 15$, and then quickly grows to 3.5 mmag at the faint end of $G \sim 17$. Table 1 presents the scatter values of the magnitude differences between the SCR and the XPSP standards at four specific magnitudes for all 12 bands.

2.3. Calibration Stars

We combine the USS DR1 photometric data with the BEST catalog using an adopted crossmatching radius of 1″. Then, we select standard stars as the calibration samples with the following constraints:

[16] https://splus.cloud/
[17] https://www.lamost.org/dr10/

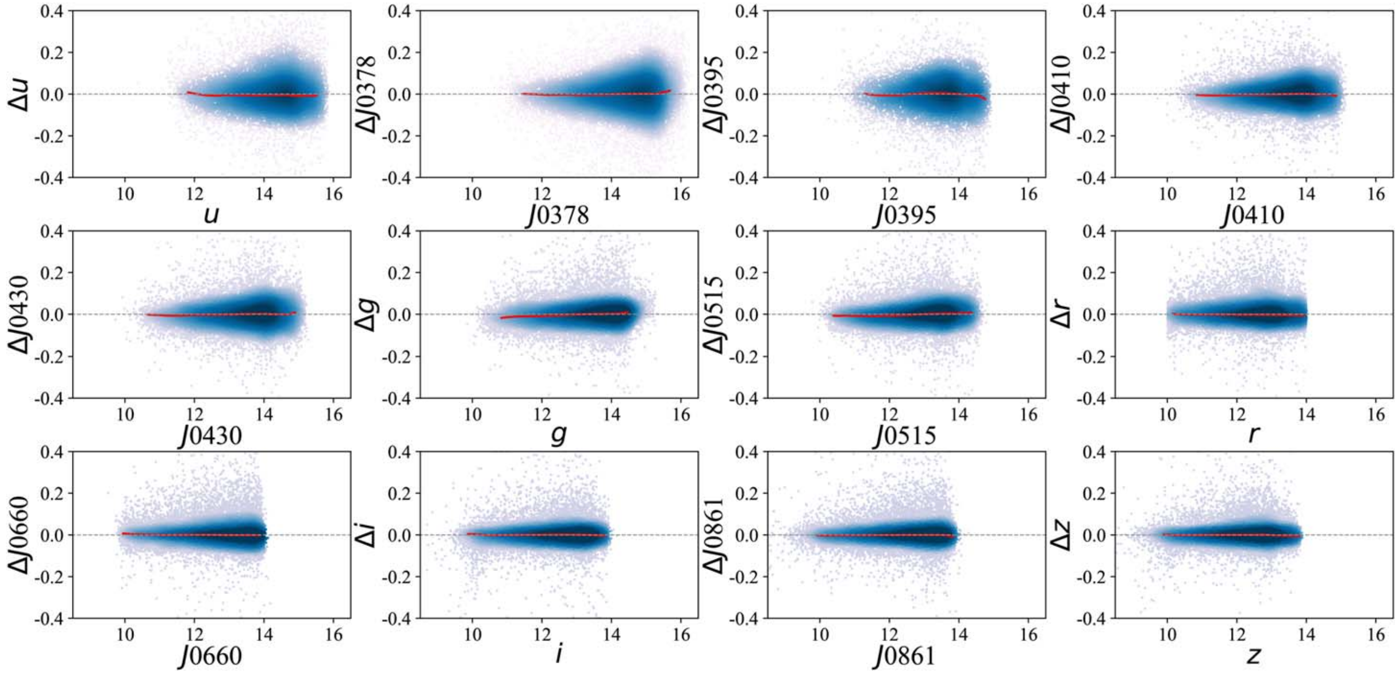

Figure 2. Variations of the magnitude offsets, as a function of USS magnitude, for all 12 bands. For each panel, the colors represent the logarithm of the number density, calculated using Gaussian kernel density estimation. The red and gray lines denote the median values and zero levels of the magnitude offsets, respectively.

Table 1
Standard Deviations of the Gaia G Magnitude Differences between the SCR and XPSP Standard Stars

Filter	$G \sim 11$	$G \sim 13$	$G \sim 15$	$G \sim 17$
$J0378$	0.0142	0.0174	0.0372	0.1329
$J0395$	0.0132	0.0155	0.0306	0.0971
$J0410$	0.0060	0.0068	0.0119	0.0322
$J0430$	0.0061	0.0067	0.0111	0.0281
$J0515$	0.0041	0.0047	0.0088	0.0219
$J0660$	0.0024	0.0032	0.0063	0.0170
$J0861$	0.0017	0.0022	0.0041	0.0111
u	0.0206	0.0213	0.0362	0.1244
g	0.0022	0.0023	0.0032	0.0074
r	0.0020	0.0020	0.0025	0.0051
i	0.0009	0.0009	0.0013	0.0035
z	0.0017	0.0019	0.0028	0.0069

(a) The magnitude in the r band is greater than 10 mag to avoid saturation, following H. D. Perottoni et al. (2024).
(b) Photometric error$\{u, J0395, J0410, J0430\} < 0.05$ mag, error$\{J0378\} < 0.08$ mag, error$\{J0515\} < 0.03$ mag, error $\{g, J0660, J0861\} < 0.02$ mag, and error$\{r, i, z\} < 0.01$ mag to maintain a balance between a good SNR and a sufficient number of photometric standard stars for each band.
(c) `SEX_FLAGS` = 0 to avoid bad USS DR1 photometry.

Finally, 26,118, 44,546, 31,395, 31,891, 37,732, 56,556, 40,081, 35,303, 81,081, 46,678, 60,970, and 38,423 calibration stars are selected in the u, J0378, J0395, J0410, J0430, g, J0515, r, J0660, i, J0861, and z bands, respectively.

3. Validation of the USS DR1 Photometric Calibration

As previously noted by B. Huang et al. (2022), systematic errors in photometric data can be mathematically expressed as functions of time, magnitude, color, and the star's position on the detector. For example, short-term variations in the Earth's atmosphere cause zero-point shifts in each observation, the nonlinearity effects of detectors (e.g., CCDs) introduce magnitude-dependent errors, the color effects of Earth's atmosphere and differences in photometric system could lead to color-related systematics, and different flat-field corrections result in errors depending on the detector position (X and Y). To precisely measure and describe potential systematic errors in USS DR1 data, we first validate dependencies of the magnitude difference between the BEST standards and the USS on magnitude, color, and detector position.

3.1. Dependence of the Magnitude Offsets on USS Magnitude and Gaia $G_{BP} - G_{RP}$ Color

The magnitude offsets between the XPSP standards and the USS, as functions of the USS DR1 magnitude and $G_{\rm BP} - G_{\rm RP}$, are shown in Figures 2 and 3, respectively. No dependence on USS magnitude is found for all bands, suggesting that the USS detector exhibits a high level of linearity. However, for the u, J0378, and g bands, a slight dependence on $G_{\rm BP} - G_{\rm RP}$ color is found, especially when the color is greater than 1.05 or less than 0.6. We attribute this effect to measurement errors in the response curve of the USS u, J0378, and g bands and/or the Gaia DR3 XP spectra. Additionally, we must consider the potential influence of extrapolating the XP spectra beyond the u band.

For the calibration of the u, J0378, and g bands, we selectively choose stars within the specific $G_{\rm BP} - G_{\rm RP}$ range of 0.6 to 1.05; less than 3% of the stars fall outside this range.

3.2. Spatially Dependent Systematics in Zero-points

To determine the zero-point offsets of the USS, we calculated the median value of the magnitude offsets between the BEST standards and the USS DR1 stars for each tile, based on the calibration stars (refer to the magnitude range in Figure 2). We note that using only very bright sources or a

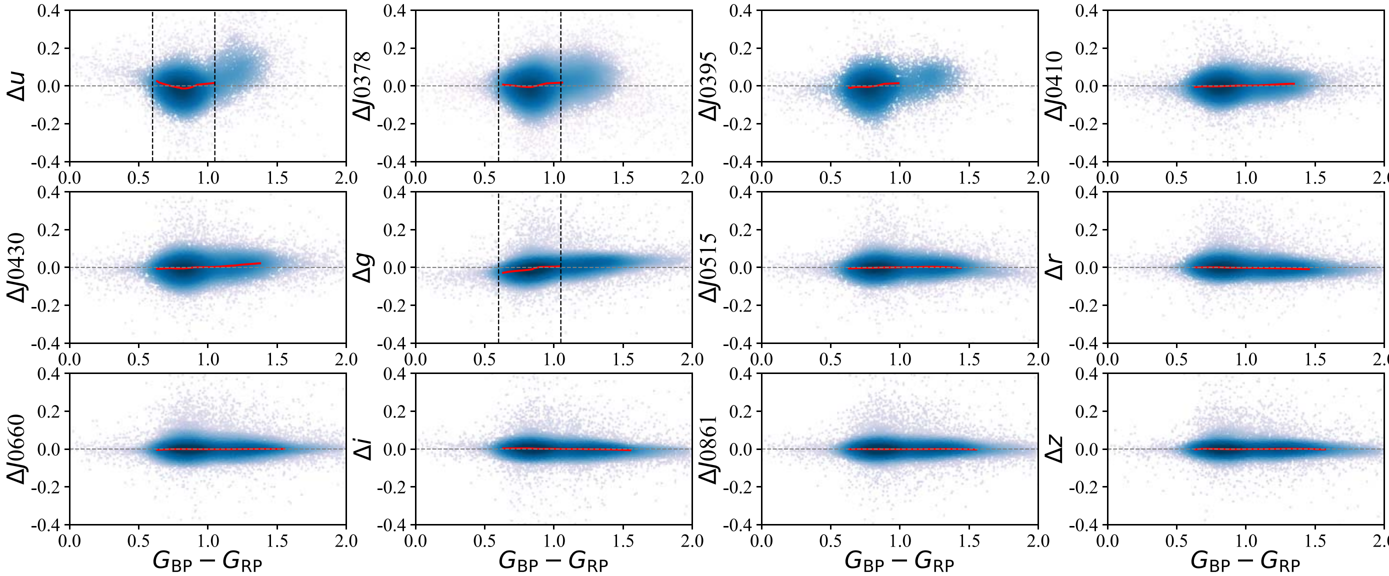

Figure 3. Same as Figure 2, but for $G_{\rm BP} - G_{\rm RP}$ color. For the u, $J0378$, and g bands, the two color cuts are denoted by black dashed lines.

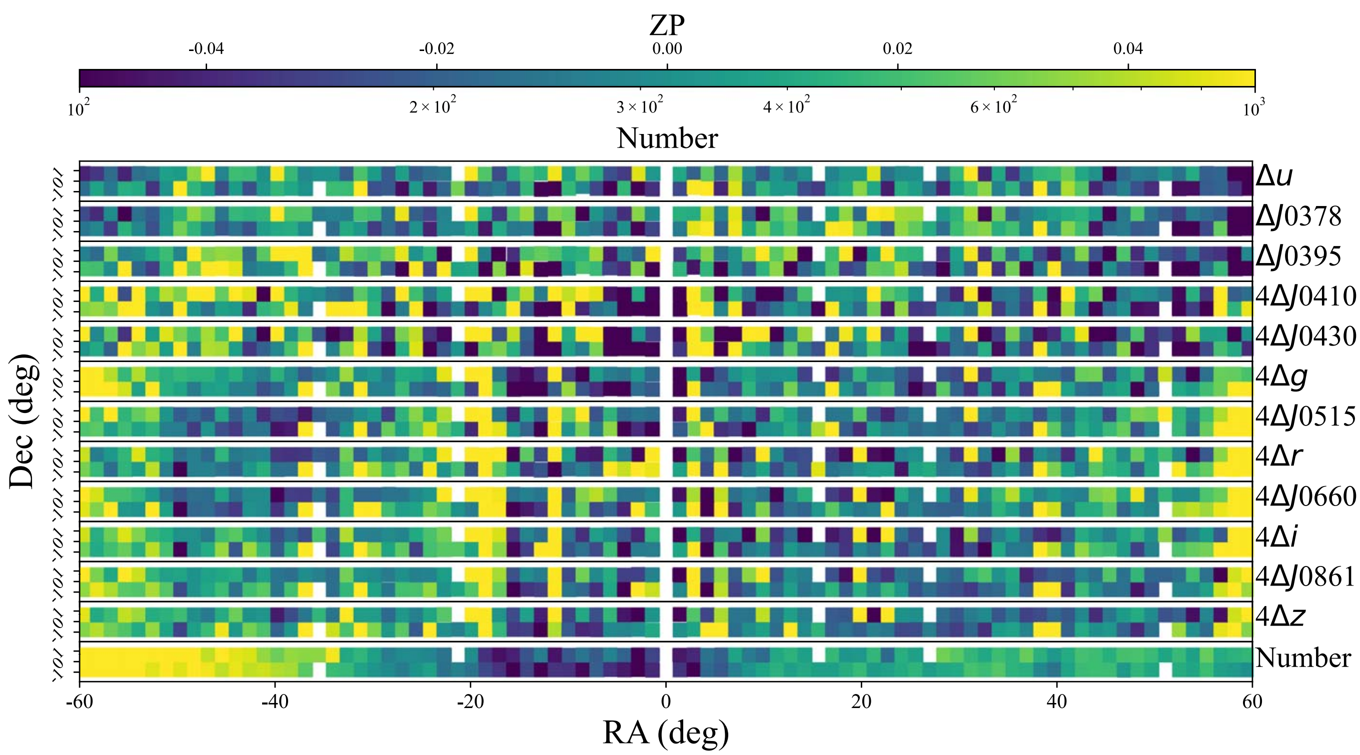

Figure 4. From top to bottom, the first 12 rows show the spatial variations of the difference between the XPSP standards and USS zero-points in each tile. The bottom row shows the distributions of the listed numbers of each tile in the r band. To clearly illustrate the spatial structure, the zero-point differences in the $J0410$, $J0430$, g, $J0515$, r, $J0660$, i, $J0861$, and z bands are multiplied by four. The labels are marked in each panel, and a color bar is shown on top.

large number of faint sources can introduce significant random errors to the zero-points. For example, the brighter the sources that are used, the fewer the standard stars that will be present in the tile, leading to a larger scatter in the zero-points. As the balance between a high SNR and a sufficient number of sources is achieved, the scatter in the zero-point will gradually stabilize and become more accurate (this work).

Figure 4 illustrates significant spatial variations in the zero-point offsets, especially for the blue filters, predominantly due to the higher uncertainties of the technique employed in the original USS DR1 calibration.

To quantitatively assess the systematic errors in the USS DR1 data, we generated histograms of the zero-point offsets between the BEST standards and USS, as shown in Figure 5. By fitting these histograms to a Gaussian function, we calculated the scatter for each filter as shown in the first line in Table 2. These results align with H. D. Perottoni et al. (2024), and suggest an internal precision of about 7–8 mmag for the *griz* filters, 12–40 mmag for the blue filters, and about 7–11 mmag for the red filters within the USS DR1 photometry.

In order to trace the systematic errors, the correlation between the zero-point offsets for each two-band filter pair is illustrated in

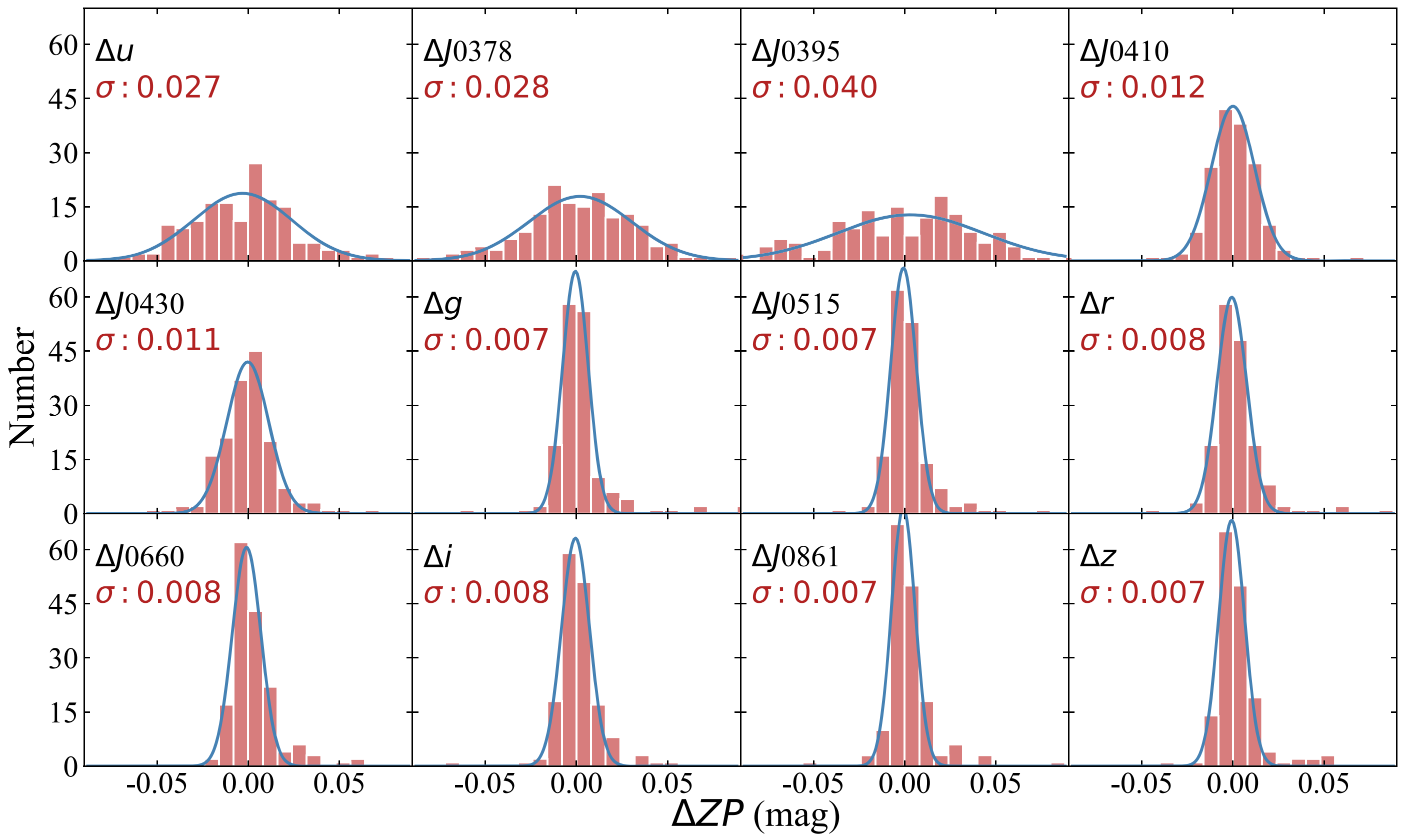

Figure 5. Histograms of the differences in zero-points between the XPSP standards and USS photometry. The bands are marked in the top-left corner of each panel. The Gaussian fitting results are plotted as blue lines. The standard deviations when using Gaussian fitting are marked in each panel in red.

Table 2
Internal Precision (in millimagnitude) of the Photometric Calibration for the 12 USS Bands before and after Recalibration

Filters	g	r	i	z	u	$J0378$	$J0395$	$J0410$	$J0430$	$J0515$	$J0660$	$J0861$
Before	7.0	8.1	7.7	7.1	26.9	28.1	39.8	11.9	11.5	7.0	7.9	6.5
After	0.7	0.7	1.0	1.0	6.4	4.6	3.8	2.0	1.5	1.1	1.2	0.6

Figure 6. The systematics typically arise from at least two sources. For the blue-band pairs (involving the u, $J0378$, $J0395$, $J0410$, and $J0430$ filters), we estimated the slope through linear fitting. This slope varies between different band pairs. A common source of those systematic errors is the inadequate handling of stellar metallicity in the SL method. The slope value reflects the ratio of metallicity sensitivities between the two bands. For example, the slopes for the $J0378$ versus $J0395$ bands and the $J0430$ versus $J0410$ bands are close to unity, because the sensitivity to metallicity is nearly identical for the $J0378$ and $J0395$ bands, and the $J0430$ and $J0410$ bands. Details on the metallicity sensitivity in the blue bands can be found in Figure A1 of K. Xiao et al. (2023c). Conversely, the slope for the $J0430$ versus u bands is 0.18, because the u band is significantly more sensitive to metallicity than the $J0430$ band. In addition, for the red-band filter pairs (e.g., the $J0515$ versus g bands), the zero-points typically align along the $y = x$ line, and present a high correlation. We believe that this systematic error is primarily due to systematic errors in ATLAS Refcat2.

3.3. Dependence of Magnitude Offsets on CCD Position

The CCD position variations in the magnitude offsets between the XPSP standards and USS DR1 (after removing the zero-level constant for each tile across all 12 bands) are shown in Figure 7. For each tile, there are significant CCD position-dependent systematic errors, reaching up to 50 mmag, with correlations observed across different bands.

To quantitatively analyze this correlation, taking the r band as an example, we randomly selected one tile (`SHORTS-STRIPE82_0090`) from all tiles where the number of XPSP standards exceeds 1000. The correlation of magnitude offsets between each pair of bands for `SHORTS-STRIPE82_0090` is plotted in Figure 8. Within the same field, magnitude offsets between different bands present correlations, with 80% of the band pairs having a linear correlation coefficient greater than 0.4. For any two bands, linear fitting was performed, and it revealed that 74% of the tiles have a slope exceeding 0.4. For example, in the $\Delta J660$ versus Δr panel, points are distributed along the $y = x$ line, with a correlation coefficient of 0.90 and a slope of 1.01. We then plotted the FWHM correlation for each pair of bands, as shown in Figure A2. For each band pair, all the points are distributed along the $y = x$ line. Furthermore, we found strong correlations in the FWHM across the different bands, and the magnitude offsets and FWHM for each band pair. We believe that the systematic errors primarily originate from the aperture correction process. Two other tiles,

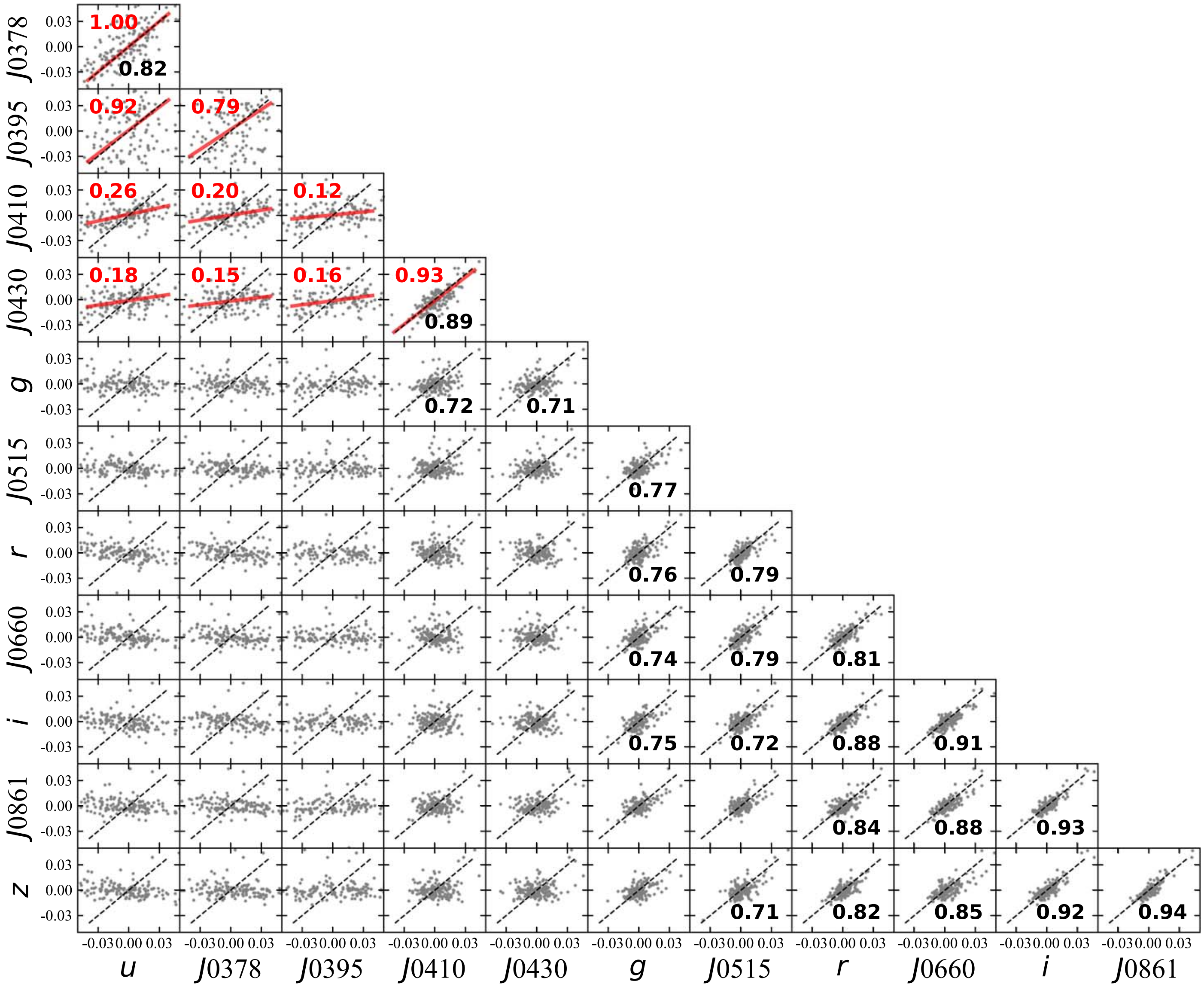

Figure 6. Correlation plots of the zero-point offsets between the BEST standards and USS photometry for each of the two bands. For each panel, the correlation coefficient is displayed in the bottom-right corner only when it exceeds 0.7. The black dashed lines denote $y = x$ in each panel. The red lines represent the results of linear fitting; the slopes are also marked in red.

SHORTS-STRIPE82_0096 and SHORTS-STRIPE82_0100, exhibit the same phenomenon.

We next selected 42 tiles with more than 700 standard stars from all r-band observations, and plotted the distribution of the difference between the XPSP and the USS magnitudes, the difference between the APER_6 and USS magnitudes, the normalized FWHM, and the ellipticity across the CCD space, as shown in Figure 9. We found that these CCD position-dependent systematic errors strongly correlate with the distribution of the difference between the APER_6 and USS magnitudes in CCD space, show a strong negative correlation with the spatial distribution of FWHM, and exhibit almost no correlation with ellipticity or the astrometric offsets with Gaia (please refer to Figure A3). This indicates that the aperture size used for USS magnitudes in the photometric process is too small to fully capture the total flux of sources having a large FWHM. Although CCD position-dependent systematic errors caused by selecting apertures that are too large or too small should be well corrected during the aperture correction process, this appears to not be the case. We remind the reader that the USS magnitudes here refer to the APER_3 magnitudes after aperture correction, as mentioned in Section 2.3.

To further quantify this correlation, we plotted the distribution of the difference between the XPSP and USS magnitudes, as a function of normalized FWHM, across the different bands for the tile SHORTS-STRIPE82_0090, as shown in Figure 10. The linear correlation coefficient is as high as 0.86, and the linear fitting results, H(FWHM), with a slope of up to 0.79, are also noted in the figure. Since the absolute reference value of the FWHM is unavailable, we used the normalized FWHM for analysis here. As is well known, the absolute FWHM for a tile is positively correlated with the median value of the aperture correction value. In other words, a tile with a larger FWHM will often have larger aperture corrections. Although the absolute FWHM is not entirely equivalent to the median value of the aperture correction for a given tile, the correlation between them is still valuable for analysis. As shown in Figure 10, panels with larger aperture corrections exhibit more pronounced variations in

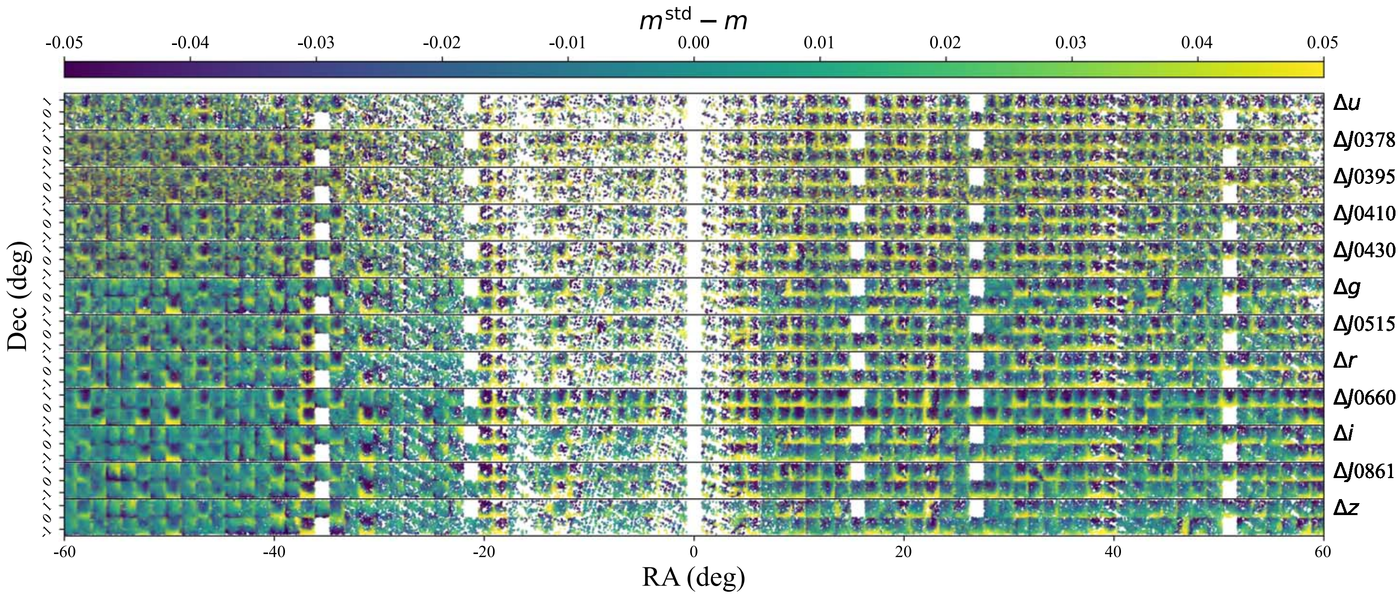

Figure 7. Same as Figure 4, but for magnitude offsets between the XPSP standards and the USS photometry after subtraction of the zero-points for each tile. The bands are marked on the right, and a color bar is shown on top. The tire-track-like structures observed in the figure, extending roughly from R.A. = −30° to 0 and related to Gaia's scanning law, are mainly caused by the spatial nonuniformity of the numbers of the Gaia XP spectra. Similar structures are also observed in the bottom-right panel of Figure 4 in K. Xiao et al. (2023b).

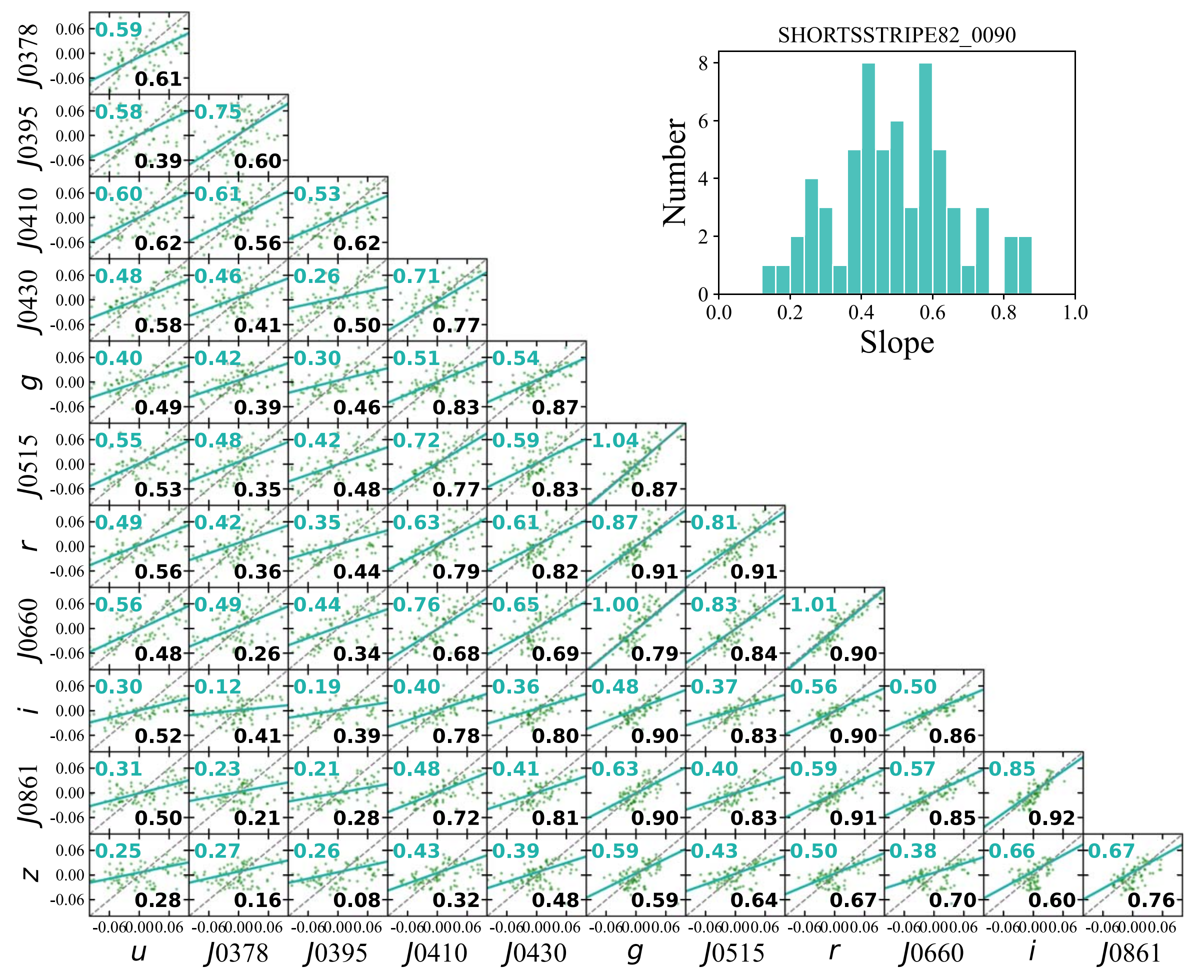

Figure 8. Same as Figure 6, but for the correlation of the magnitude offsets between the standards and USS photometry after subtraction of zero-points for `tile_ID=SHORTS-STRIPE82_0090` for each of the two bands. For each panel, the correlation coefficients are marked in the bottom-right corners. The linear fitting lines are shown as light-green lines, and the slopes of the lines are marked in the top-left corners. The black dashed lines denote $y = x$ in each panel. A histogram of the distribution of the slopes is shown in the top-right corner.

Figure 9. Examples of the spatial variations of the magnitude offsets between the XPSP standards and USS r-band photometry (the top-left panel), the magnitude offsets between the USS r-band magnitudes with aperture 6 and aperture 3 after aperture correction (the top-right panel), the normalized FWHM (the bottom-left panel), and ellipticity (the bottom-right panel). For the bottom-right panel, the points are displayed after removing the median of all points in the tile, and the median value is marked (in gray) in the top-right corner for each tile. The `tile_ID` is marked in each tile in black. The color bars are shown on top of the panels.

stellar magnitude differences with changes in the normalized FWHM (e.g., panels 119 and 101). In contrast, the variations are more subdued in plots with larger aperture corrections (e.g., panels 99 and 118).

Using the linear fitting results, we then corrected the FWHM-dependent systematic errors for all 42 tiles. The corrected results are shown in the left panel of Figure 11. After correction, the residuals still exhibit a moderate dependence on CCD position. The spatial distribution of the residual errors closely mirrors that of the difference between the XPSP and USS `APER_6` magnitudes, shown in the right panel of Figure 11. The residual errors are primarily attributed to a different flat-field correction.

Furthermore, for each tile, we fitted the residuals after correcting for FWHM-dependent systematic errors using a second-order two-dimensional polynomial (with six free parameters), as a function of X and Y. The results of the second-order two-dimensional polynomial fitting, $F(X, Y)$, for all 42 tiles are shown in the left panel of Figure 12. We then applied these polynomials to each tile to correct the residual errors; the corrected residuals are presented in the right panel of Figure 12. It is notable that, for each panel, the spatial structure of the residuals exhibits an intermediate-scale pattern between large-scale and small-scale flat fields, and remains nearly consistent across different tiles. To illustrate this intermediate-scale structure more clearly, we combined the residuals of the 42 tiles, and plotted the results in the left panel of Figure 13. To avoid overcrowding, 400 bins were uniformly selected in the CCD space, and the median value of the residuals within each bin was used as the value for that bin. This smoothed result is displayed in the right panel of Figure 13. A mottling pattern, reaching up to 40–50 mmag for the u-, $J0378$-, $J0395$-, $J0410$-, and $J0430$-band filters, and 10–20 mmag for the other filters, is clearly visible. This

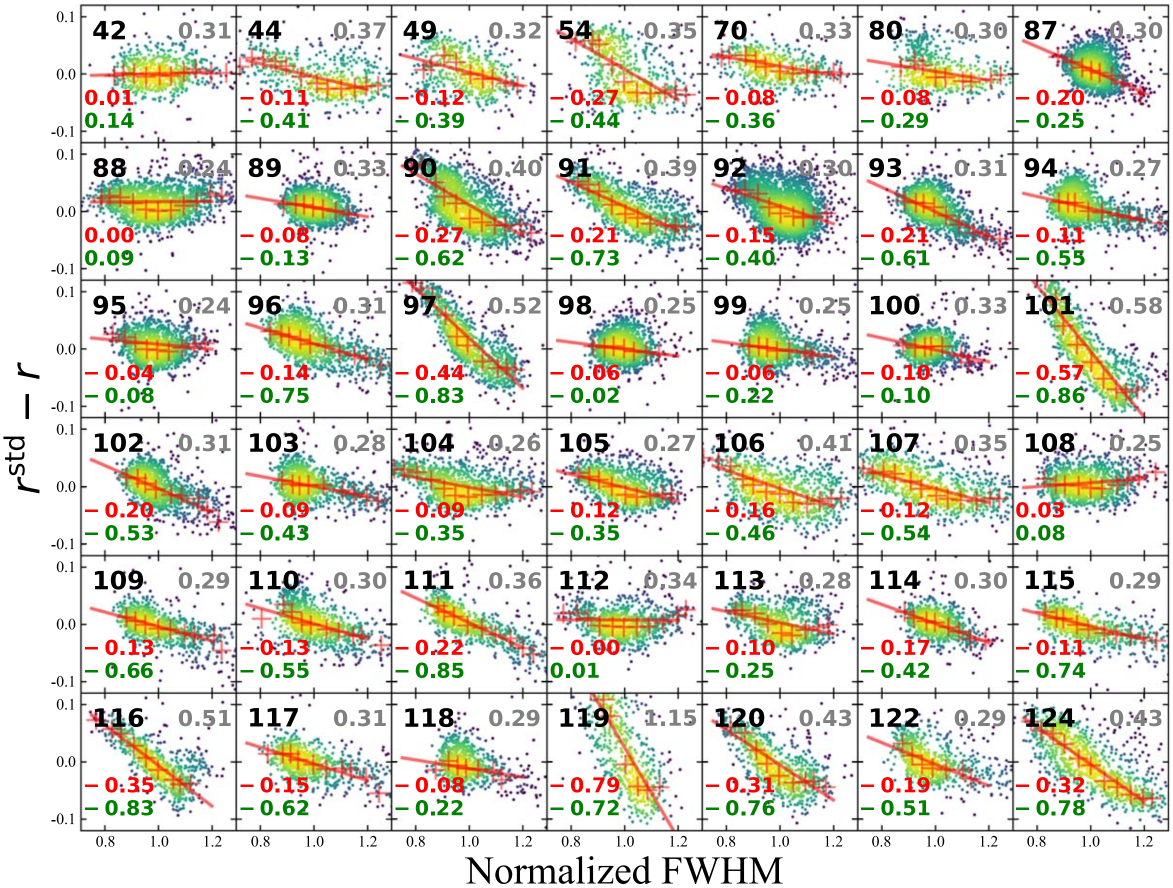

Figure 10. Examples of correlation plots of the magnitude offsets between the standards and the USS r-band photometry, as a function of the normalized FWHM. For each panel, the red plus signs denote the median values of the points, and the red lines denote the linear fitting result to the red pluses. The `tile_ID` (black), the correlation coefficient (green), and the slope (red) are marked in each panel. The gray number in each panel represents the magnitude offset in the aperture correction process.

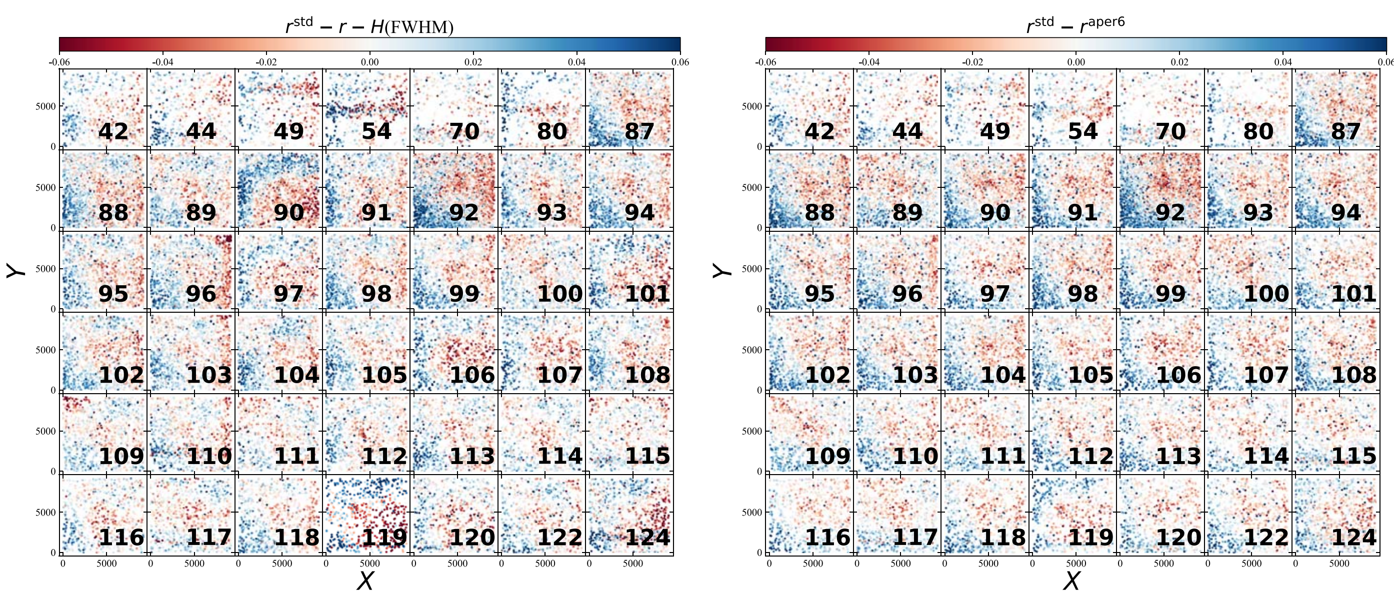

Figure 11. Examples of the stellar flat field in the r band. Left panel: spatial variations of the magnitude offsets between the standards and USS r-band photometry after FWHM-dependent systematic error correction using a second-order two-dimensional polynomial (with six free parameters) fitting. The `tile_ID` is marked in each tile in black. Right panel: spatial variations of the magnitude offsets between the standards and USS r-band magnitude with `APER_6`. The color bars are shown on top.

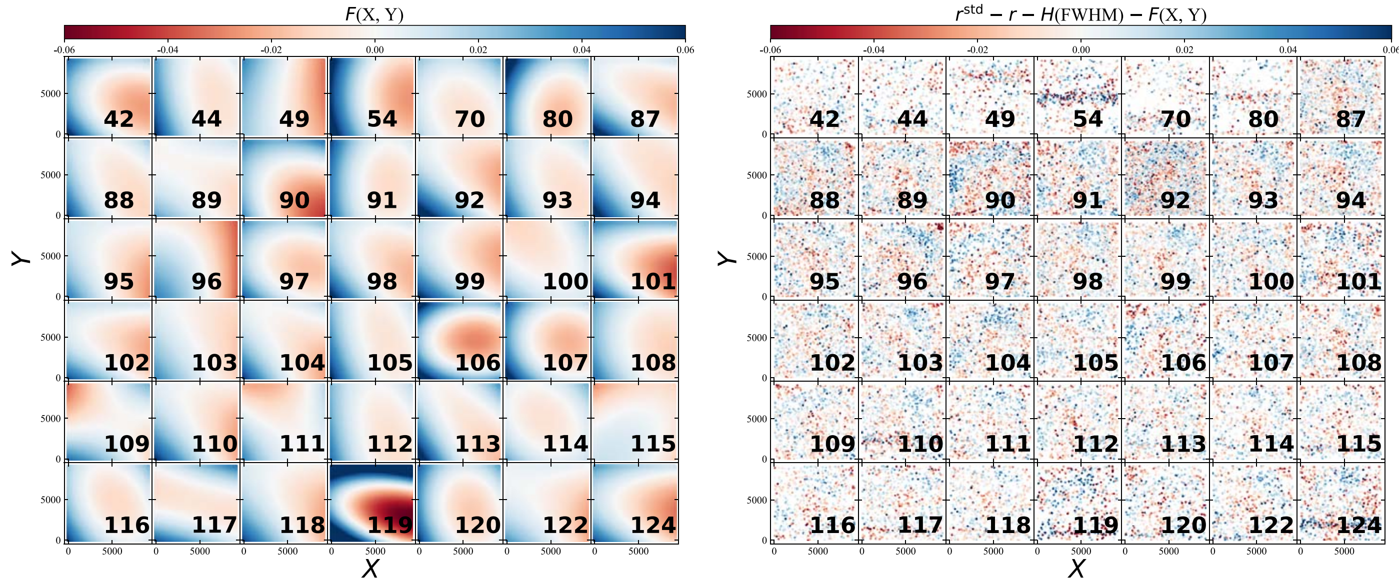

Figure 12. Examples of the medium-scale stellar flat field in the r band. The color bars are shown on top. Left panel: spatial variations of the magnitude offsets between the standard and USS photometry after FWHM- and large-scale stellar flat-field correction. The `tile_ID` is marked in each tile in black. Right panel: residuals after application of the second-order two-dimensional polynomial.

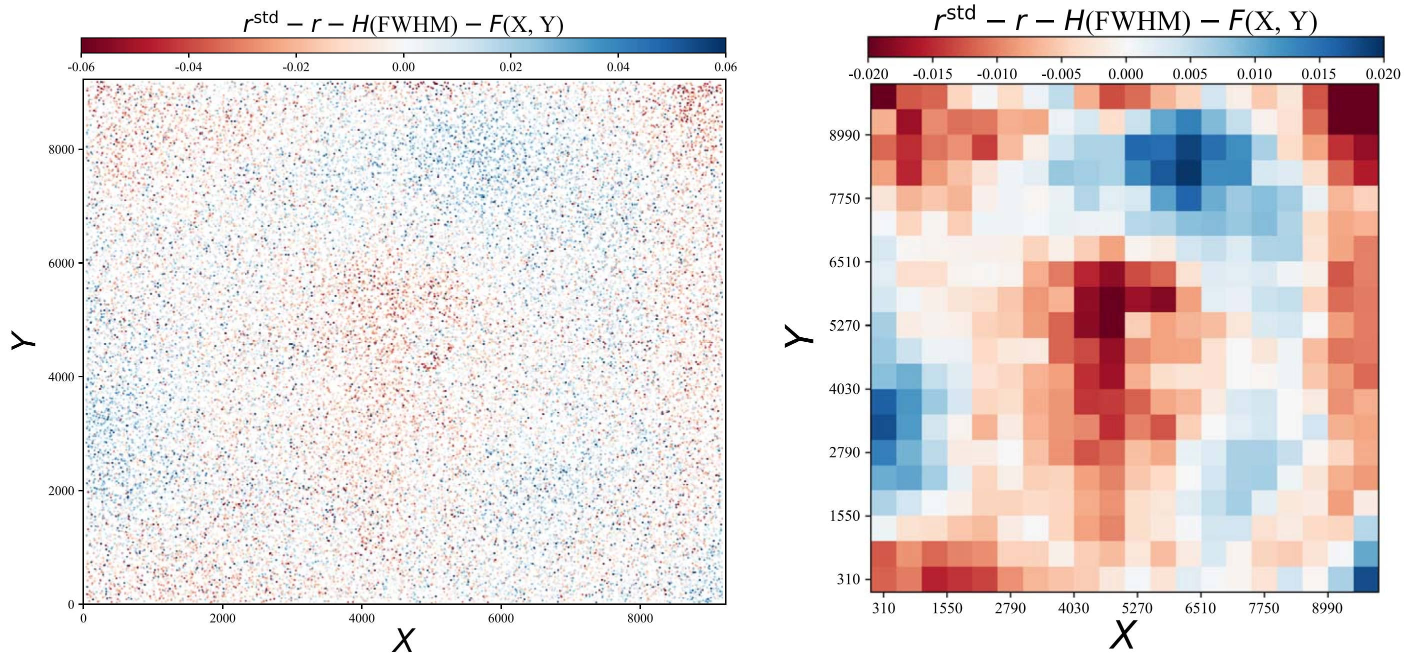

Figure 13. Spatial variations of the second-order two-dimensional polynomial fitting residuals of the 42 tiles (left panel) and the results after 20 × 20 binning (right panel). The color bars are shown on top.

intermediate-scale structure is widely found in modern survey data, such as SAGES DR1 (refer to Figure 7 in K. Xiao et al. 2023a), J-PLUS DR3 (depicted in Figure 15 in K. Xiao et al. 2023c), and S-PLUS iDR4 (see Figure 10 in K. Xiao et al. 2024b). A detailed description of this intermediate-scale structure is presented in Section 6.4 below.

4. Systematic Error Corrections

Section 3 highlights the spatially dependent systematic errors in the zero-points of the USS photometry, as well as systematics resulting mainly from different aperture and flat-field corrections. Both the systematic errors from the aperture correction process and those from the flat-field correction process can be modeled as functions of the CCD position (X, Y).

To accurately correct for these systematic errors in the USS data, we first applied a second-order two-dimensional polynomial, as a function of CCD position (X and Y), fit to the difference between the standard star magnitudes ($m^{\rm std}$), including the SCR and the XPSP standards, and the USS magnitudes (m) for each tile. For the ith band and jth tile, the second-order two-dimensional polynomial is expressed as

$$\mathcal{F}_{i,j} = a_{i,j}^{0} \cdot X^2 + a_{i,j}^{1} \cdot Y^2 + a_{i,j}^{2} \cdot X \cdot Y + a_{i,j}^{3} \cdot X + a_{i,j}^{4} \cdot Y + a_{i,j}^{5}.$$

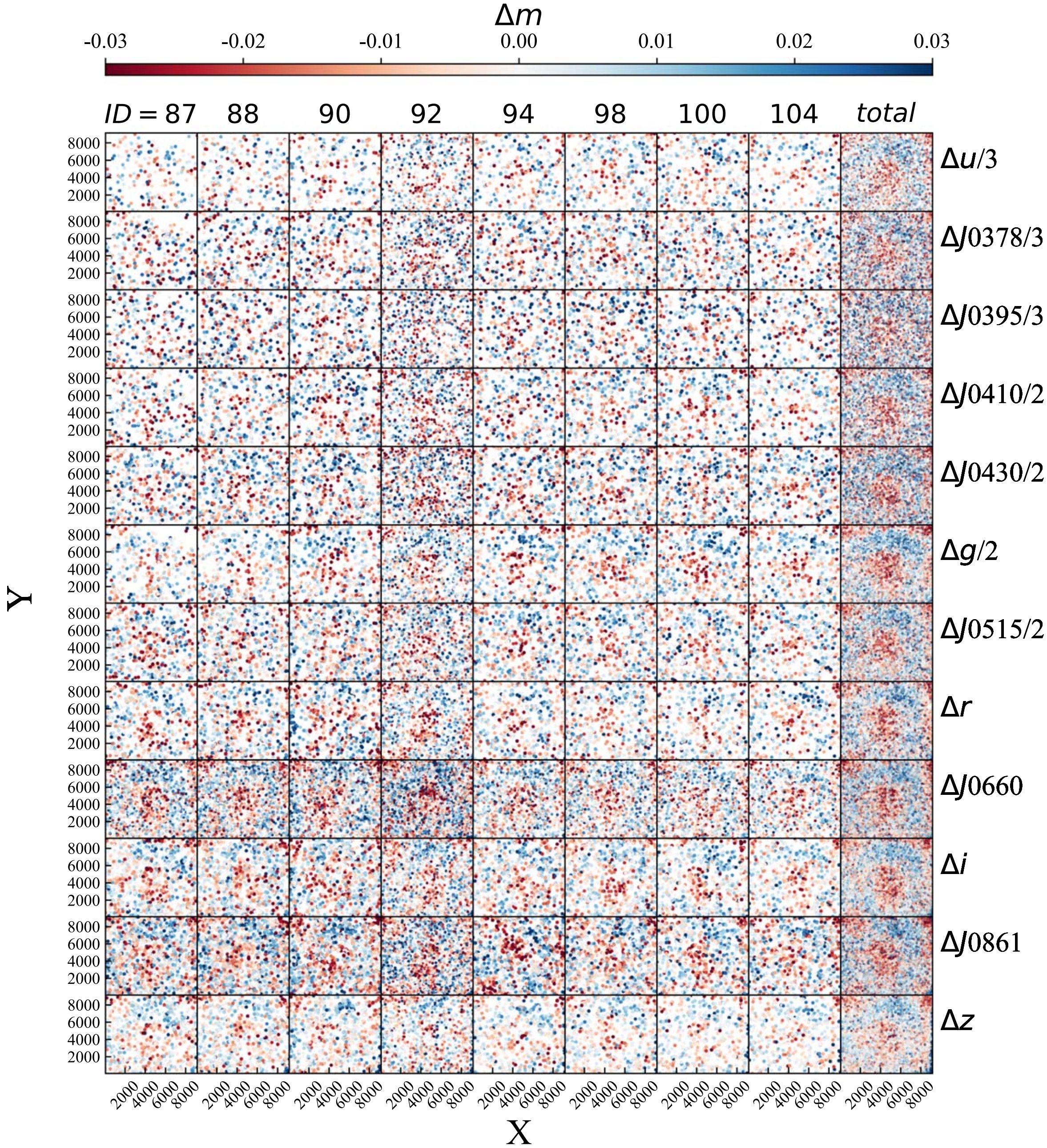

Figure 14. An example showing the CCD spatial distribution of residuals after applying the second-order two-dimensional polynomial correction. The panels, arranged from top to bottom, display the u, $J0378$, $J0395$, $J0410$, $J0430$, g, $J0515$, r, $J0660$, i, $J0861$, and z bands. The bands are labeled on the right, and a color bar is provided on top. From left to right, the first eight columns represent the selected eight tiles (`SHORTS-STRIPE82_0087`, `SHORTS-STRIPE82_0088`, `SHORTS-STRIPE82_0090`, `SHORTS-STRIPE82_0092`, `SHORTS-STRIPE82_0094`, `SHORTS-STRIPE82_0098`, `SHORTS-STRIPE82_0100`, and `SHORTS-STRIPE82_0104`), with the final column showing the combined residuals of these eight tiles. The tile number is indicated between the first-row panels and the color bar. To clearly show the spatial structure, the results for the u, $J0378$, $J0395$, $J0410$, $J0430$, g, and $J0515$ bands are compressed by two to three times.

Here, $a_{i,j}^0$, $a_{i,j}^1$, $a_{i,j}^2$, $a_{i,j}^3$, $a_{i,j}^4$, and $a_{i,j}^5$ represent six free parameters for the ith band and jth tile.

These polynomial coefficients were then used to correct for large-scale structures in the CCD spatial and zero-point offsets in each tile. We required that, for each band and tile, the number of standard stars exceed 20, ensuring more data points than polynomial coefficients.

After applying the second-order two-dimensional polynomial correction, Figure 14 shows the CCD spatial distribution of residuals for eight tiles, each with a relatively high number of calibration stars, across all 12 bands. Different tiles exhibit a consistent mottling structure within the same band, and different bands display a similar pattern for the same tile. This suggests that the medium-scale flat-field structure remains consistent across bands and over short timescales, and also indicates that the second-order polynomial correction effectively corrects CCD position-dependent systematic errors from both different aperture and different flat-field corrections in the USS DR1 photometric data.

Although a carefully modeled radial function, constructed with a basis function of $f(\sqrt{X^2 + Y^2})$, could correct part of the mottling pattern in the USS DR1 data, a more effective approach for general cases would be to use the numerical stellar

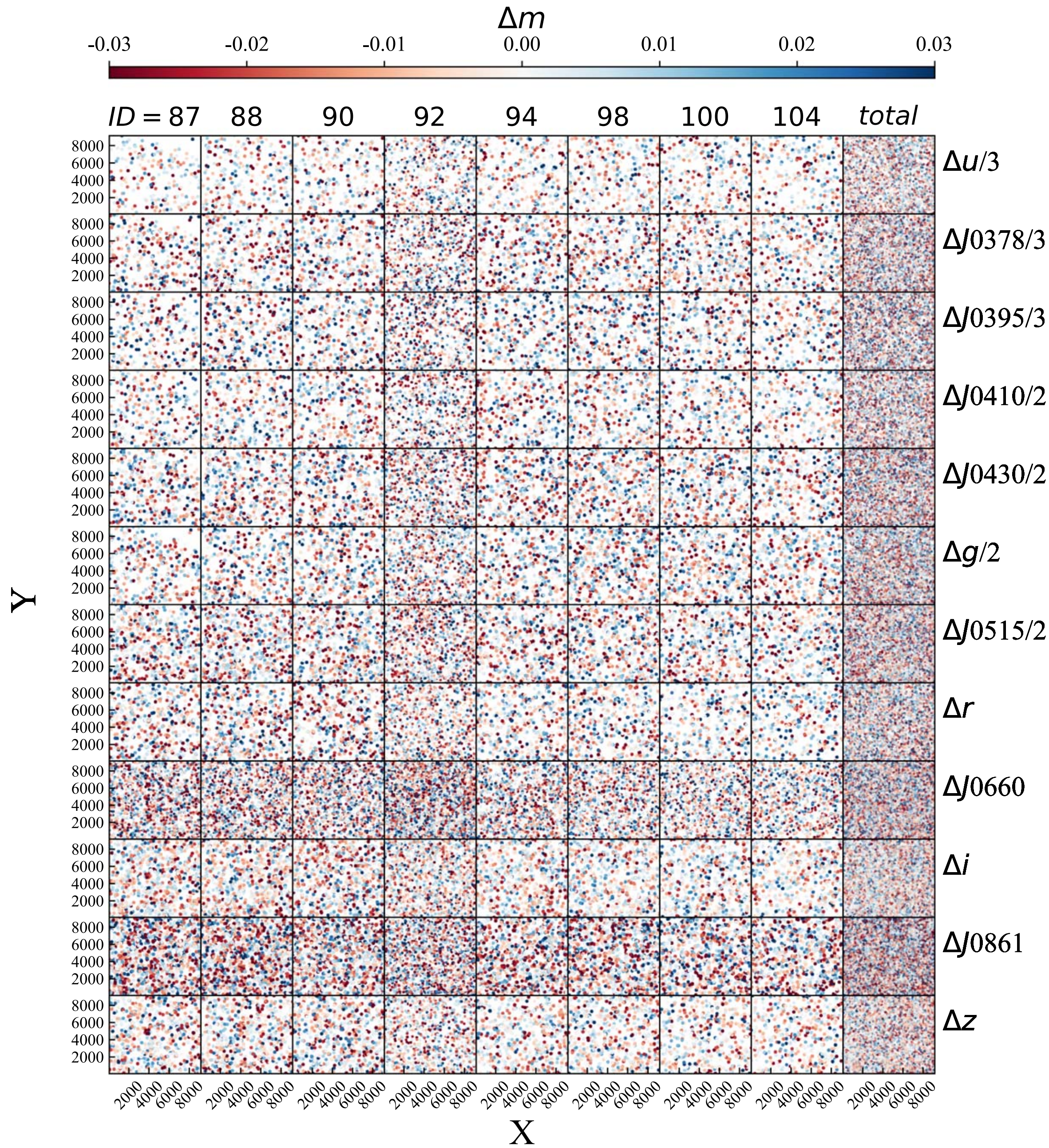

Figure 15. Similar to Figure 14, but showing the results after applying both second-order two-dimensional polynomial and numerical stellar flat-field corrections.

flat-field correction method discussed in K. Xiao et al. (2024b). The medium-scale CCD position-dependent systematic errors are then corrected using the numerical stellar flat-field correction method for each tile.

The difference between the XPSP standards and the USS magnitudes, after applying both second-order two-dimensional polynomial and numerical stellar flat-field corrections, is shown in Figure 15. It is evident that, following recalibration, the photometric data are significantly more uniform. For example, for `SHORTS-STRIPE82_0092`, the consistency of the USS r-band photometry improves from 27 to 8.9 mmag.

When using the recalibrated USS DR1 photometric data, one can download the FITS file `Recalibrated_USS_DR1_Photometry.fits` from ChinaVO at doi:10.12149/101503. This file contains 96 columns, with each band containing the following eight columns: R.A. (`RA_band`), decl. (`DEC_band`), original aperture magnitude after aperture correction (`band_PStotal`), magnitude error (`band_err_PStotal`), photometric quality flag (`band_flag`), stellar probability (`band_class_star`), aperture magnitude after second-order two-dimensional polynomial stellar flat-field correction (`band_PStotal_D2O2`), and the final calibrated aperture magnitude (`band_PStotal_corr_final`) that accounts for numerical stellar flat-field correction.

5. Recalibration Precision in the Zero-points

The XPSP standard stars are derived from the corrected Gaia XP spectra, while the SCR standard stars, based on atmospheric parameters from LAMOST and Gaia photometry, are predicted with an independent approach. In the absence of an

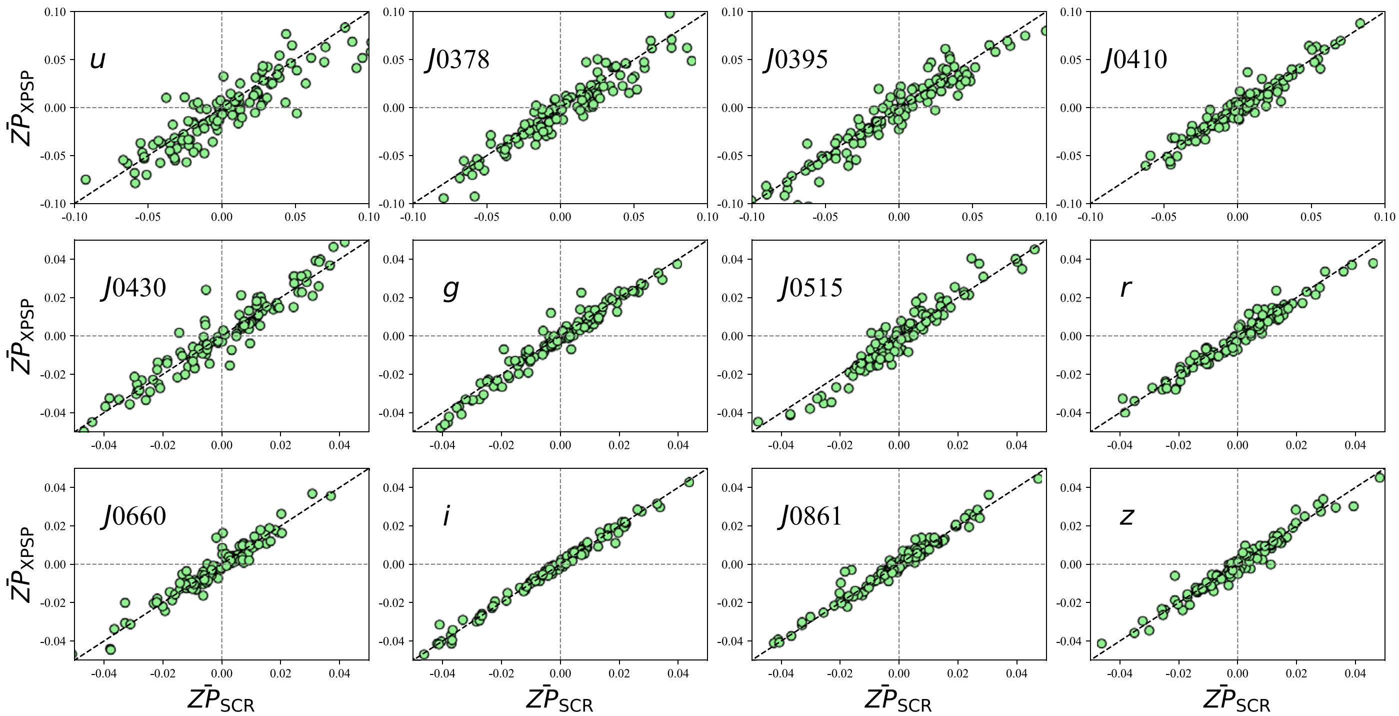

Figure 16. Correlation plots between the zero-point offsets predicted by the XPSP and the SCR standard stars for all bands. For each panel, the bands are marked in the top-left corner. The black dashed lines denote $y = x$ in each panel; the gray dashed lines denote the zero level.

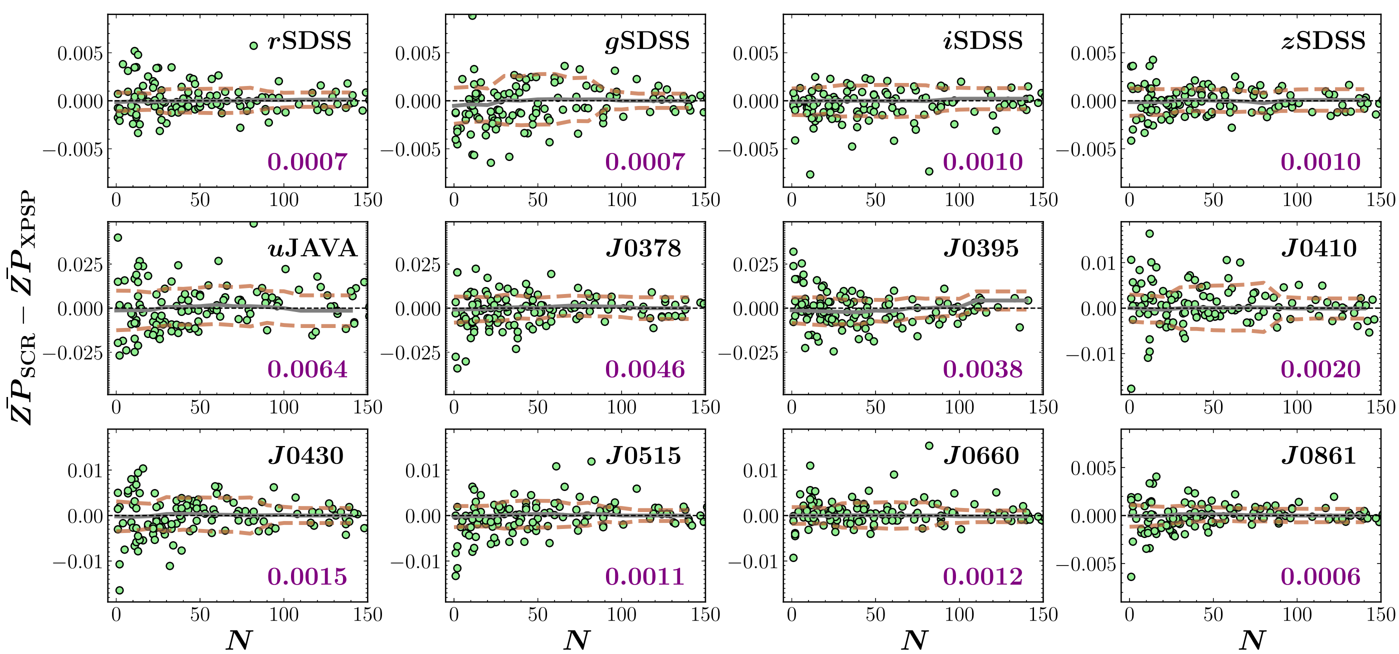

Figure 17. Comparison of the zero-points for each of the SCR and XPSP standard stars for all 12 bands, as a function of star numbers (denoted as N) in each tile. The bands are marked in each panel. The green points show the difference of the zero-points. Their median values and standard deviations are estimated using Gaussian fitting with a running width of 15 stars and a running step of one star, and are indicated by the gray solid and red dashed curves, respectively. The median value of the standard deviations, for N ranging from 100 to 150, is labeled in each panel. The black dashed lines represent the zero-residual line. The distribution of zero-point differences is not strictly symmetric about zero at intermediate and/or large N, primarily due to the limited number of fields that the zero-points have in common. However, the decreasing trend of scatter with increasing N is clearly seen in all bands.

"absolute reference," the consistency of the recalibration zero-points obtained from these two types of standard stars provides a reasonable estimate of the zero-point precision for the recalibrated USS DR1 data.

A comparison of zero-points between the XPSP and the SCR standards for all bands is shown in Figure 16. We can see that all the points are consistently distributed along the $y = x$ line for each filter. Also, the bluer the filter, the larger the scatter. To quantitatively estimate the consistency, Figure 17 displays the zero-point differences between the XPSP and SCR standards, as a function of the numbers of standard stars in each tile. For each band, the standard deviations initially exhibit higher

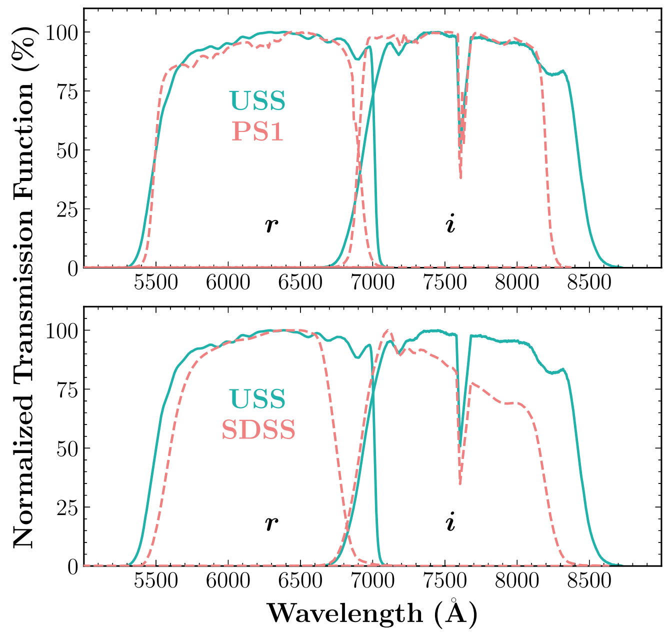

Figure 18. Normalized transmission functions, as a function of wavelength, for the r and i bands. The labels are marked in each panel. The green curves denote the USS system transmission curves. For the top panel, the pink dashed curves denote the PS1 photometric transmission curves. For the bottom panel, the pink dashed curves denote the SDSS system transmission curves.

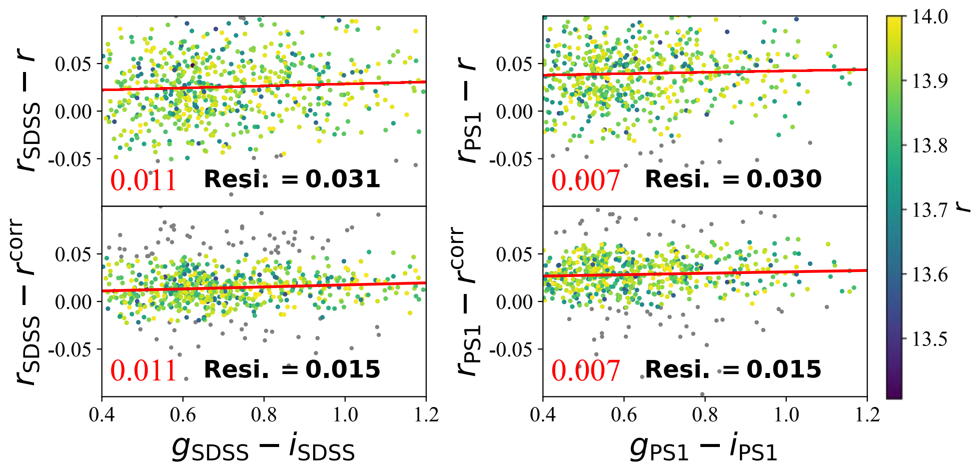

Figure 19. An example showing the difference between the SDSS and USS r-band magnitudes before (the top-left subpanel) and after recalibration (the bottom-left subpanel), and between the PS1 and USS r-band magnitudes before (the top-right subpanel) and after recalibration (the bottom-right subpanel). For each subpanel, the red line represents the result of linear fitting; the slope (red) and the standard deviation of the residuals (black) are indicated. A color bar coding the USS r-band magnitudes is shown on the right.

values, then quickly decrease and slowly converge to a stable value as the star numbers increase. The stable value, about 4–6 mmag for the blue filters and roughly 1–2 mmag for the others (as shown in the second line of Table 2), represents the final zero-point precision of the recalibrated USS DR1 photometry.

6. Discussion

6.1. Validation of the Recalibrated USS Photometry with SDSS Stripe 82 and PS1 Photometry

To evaluate the effectiveness of the photometric recalibration, we independently validate the recalibrated USS photometry using the "corrected" PS1 DR1 photometry[18] (please refer to K. Xiao & H. Yuan 2022; K. Xiao et al. 2023b) and the "corrected" SDSS Stripe 82 standard star catalog[19] (v2.6; see B. Huang & H. Yuan 2022), focusing on the r and i bands. Figure 18 shows the normalized transmission functions of the r- and i-band filters for the USS, PS1, and SDSS systems, as a function of wavelength. The USS r and i bands are very similar to the SDSS and PS1 bands.

We combine the recalibrated USS DR1 photometric data with the PS1 DR1 and SDSS Stripe 82 standard catalog with a crossmatching radius of 1″. Then we select stars with USS r-band magnitudes greater than 10 and less than 14, as well as with `SEX_FLAGS` = 0, resulting in a total of 723 stars. For each band, four colors, $m_{\rm SDSS} - m^{\rm corr}$, $m_{\rm PS1} - m^{\rm corr}$, $m_{\rm SDSS} - m$, and $m_{\rm PS1} - m$, are adopted. Here, $m_{\rm SDSS}$, $m_{\rm PS1}$, m, and $m^{\rm corr}$ represent

[18] https://nadc.china-vo.org/bestphot/

[19] https://faculty.washington.edu/ivezic/sdss/catalogs/stripe82.html

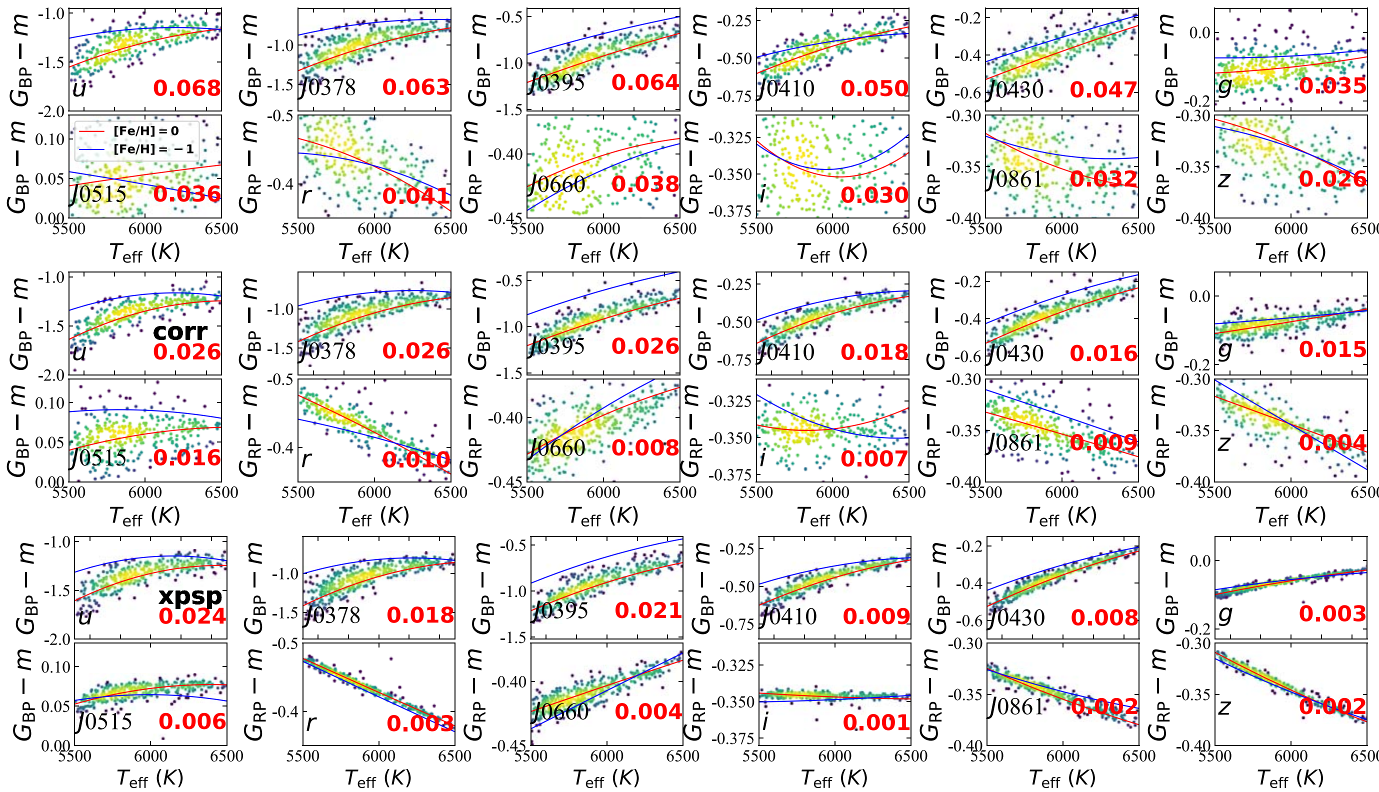

Figure 20. Polynomial fits of the intrinsic colors, with respect to $T_{\rm eff}$ and [Fe/H], for the selected stars. For each panel, the colors of the points represent the logarithm of the number density, calculated using Gaussian kernel density estimation. The fit results after 3σ clipping are shown in each panel, with the red and blue curves representing results for [Fe/H] = 0 and [Fe/H] = −1, respectively. The fitting residuals are labeled in red. The stellar color is predicted by $G_{\rm BP/RP} - m$, where m denotes the USS magnitude before recalibration (the top 12 panels), the USS magnitude after recalibration (the middle 12 panels), or the USS XPSP magnitude (the bottom 12 panels).

the m-band magnitudes of SDSS Stripe 82, PS1, and the USS DR1 magnitude before and after recalibration, respectively. Next, a linear polynomial, as a function of $g_{\rm SDSS} - i_{\rm SDSS}$ and $g_{\rm PS1} - i_{\rm PS1}$, is used to fit the colors $m_{\rm SDSS} - m$ or $m_{\rm SDSS} - m^{\rm corr}$, and $m_{\rm PS1} - m$ or $m_{\rm PS1} - m^{\rm corr}$, respectively.

The final fitting results for the r band are presented in Figure 19. Before photometric recalibration, the fitting residuals are 31 mmag for SDSS Stripe 82 and 30 mmag for PS1; after recalibration, they significantly decrease to about 15 mmag, indicating a twofold precision improvement in the recalibration process. A similar phenomenon is also observed for the i band. We ignore the effect of extinction in this process, as the extinction values for USS stars are small ($E(B-V) \leqslant 0.068$), and the differences of the r- or i-band filters between the USS, PS1, and SDSS are minimal, resulting in a low reddening coefficient (less than 0.02; estimated from R. Zhang & H. Yuan 2023; K. Xiao et al. 2024b) in the $r_{\rm SDSS} - r$, $r_{\rm PS1} - r$, $i_{\rm SDSS} - i$, and $i_{\rm PS1} - i$ colors.

6.2. Validation of the Recalibrated USS Photometry with LAMOST and Gaia Photometry

In this subsection, we describe a comprehensive evaluation across all 12 bands. We combine the USS photometry with the LAMOST DR10 and Gaia EDR3 photometry corrected by L. Yang et al. (2021), using a crossmatching radius of 1″. We then select a low-extinction sample with $E(G_{\rm BP} - G_{\rm RP}) \leqslant 0.02$, applying the same criteria to the SCR standard stars and the calibration stars. Ultimately, a total number of 316, 382, 315, 309, 332, 368, 319, 292, 387, 298, 329, and 277 stars are selected for the u, $J0378$, $J0395$, $J0410$, $J0430$, g, $J0515$, r, $J0660$, i, $J0861$, and z bands, respectively.

For each USS magnitude, both before and after photometric recalibration, as well as for the XPSP standard photometry, 12 intrinsic colors are determined, following K. Xiao et al. (2024b). A second-order two-dimensional polynomial, as a function of $T_{\rm eff}$ and [Fe/H], is then employed to fit the intrinsic colors.

The final fitting results are presented in Figure 20. Before photometric recalibration, the standard deviations of the fitting residuals are 68, 63, 64, 50, 47, 36, 38, 32, 35, 41, 30, and 26 mmag for the $G_{\rm BP} - u$, $G_{\rm BP} - J0378$, $G_{\rm BP} - J0395$, $G_{\rm BP} - J0410$, $G_{\rm BP} - J0430$, $G_{\rm BP} - J0515$, $G_{\rm RP} - J0660$, $G_{\rm RP} - J0861$, $G_{\rm BP} - g$, $G_{\rm RP} - r$, $G_{\rm RP} - i$, and $G_{\rm RP} - z$ colors, respectively. After recalibration, the standard deviation of the fitting residuals significantly improves, decreasing to approximately 16–26 mmag for the blue filters and 4–15 mmag for the other filters, representing a two- and sixfold improvement, respectively.

6.3. Precision Comparison between Recalibrated USS DR1 Photometry and XPSP Standard Stars

The recalibrated USS DR1 photometry not only enables research that requires high precision, such as metallicity measurements based on photometry (see, e.g., Y. Huang et al. 2024), but also offers the possibility for precise photometric calibration of future USS observations. Thus, we are particularly interested in comparing the precision of the

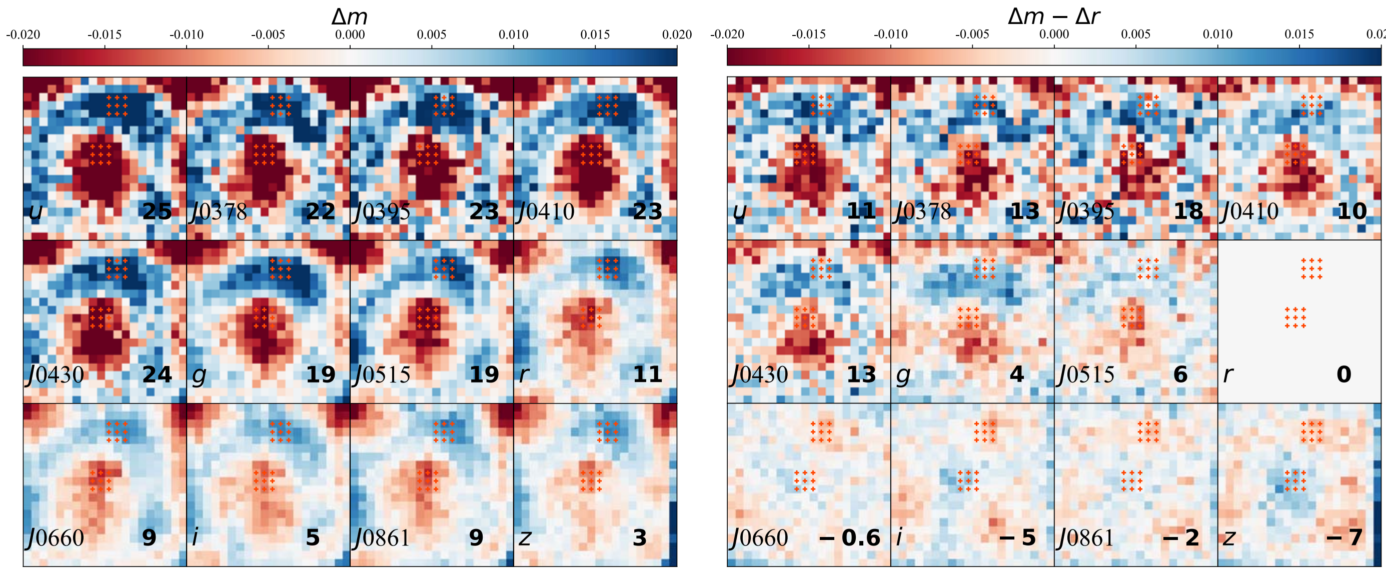

Figure 21. The left panel shows the spatial variations of the medium-scale flat field after 20 × 20 binning for all bands. The right panel is similar to the left panel, but displays the difference between the results of each band and those of the r band. The bands and color bars are shown in the bottom-left corner of each subpanel and at the top of each panel, respectively. Nine adjacent points from the annular and central regions for each band are selected and marked with red plus signs in each panel. The difference between the median values of the two regions, in units of millimagnitude, is calculated and indicated in the bottom-right corner of each subpanel.

recalibrated USS data with that of XPSP to ascertain which is superior.

The fitting results of the intrinsic colors, derived from Gaia photometry and the XPSP standards in the USS system, as a function of $T_{\rm eff}$ and [Fe/H], are shown in the bottom panels of Figure 20. The standard deviation of the fitting residuals is approximately 10–30 mmag for the blue filters (u, J0378, J0395, J0410, and J0430) and 1–6 mmag for the other filters, based on the Gaia photometry and LAMOST spectroscopic data. Our results show that the precision of individual stars for the recalibrated data in the u, J0395, and z bands is comparable to that of the XPSP standard stars, while the precision in the other bands is significantly lower.

6.4. The Medium-scale Flat-field Structure

This section provides a detailed description of the wavelength dependence and the correlation across different bands of the medium-scale flat-field structure. The medium-scale flat-field structure, representing the CCD spatial distribution of the difference between the XPSP and USS magnitudes after second-order polynomial correction, is characterized by 400 points per band, with the CCD space divided into 20 × 20 bins and the median value used for each bin.

The left panel of Figure 21 shows the distribution of the medium-scale flat-field structure in the CCD space across the 12 bands. This structure is more pronounced at the blue filters, having shorter wavelengths, and weakens as the wavelength increases. To quantify this, we select nine adjacent points from the annular and central regions for each band, and calculate the median difference between these two regions. The median differences are 25, 22, 23, 23, 24, 19, 19, 11, 9, 5, 9, and 3 mmag for the u, J0378, J0395, J0410, J0430, g, J0515, r, J0660, i, J0861, and z bands, respectively. To better illustrate this dependence, we subtract the medium-scale structure of the r band from that of the other bands, as shown in the right panel of Figure 21. The median differences between the two regions, after subtracting the r-band structure, are 11, 13, 18, 10, 13, 4, 6, 0, −0.6, −5, −2, and −7 mmag for the u, J0378, J0395, J0410, J0430, g, J0515, r, J0660, i, J0861, and z bands, respectively.

To investigate the correlation of the medium-scale structure across different bands, we plot the correlation of the 400 points between various band pairs, as shown in Figure 22. An obvious correlation is observed for each band pair. We then calculate the linear correlation coefficients; their histogram distribution is also displayed in the top-right corner of Figure 22. Approximately 79% of the band pairs have a linear correlation coefficient greater than 0.8. Furthermore, band pairs with adjacent central wavelengths exhibit points that are nearly symmetrically distributed around the $y = x$ line, while band pairs with more distant central wavelengths show some inclination. To quantify this relationship, we perform linear fitting for each band pair; the fitting results are also presented in Figure 22. The closer the central wavelengths of the band pairs are, the closer the fitting slope is to 1. Otherwise, it approaches 0. The slope indicates the relative strength of the medium-scale structure between the bands in each band pair.

7. Summary and Conclusions

In this work, we independently validated the USS DR1 photometric calibration using 30,000–70,000 carefully selected standard stars from the BEST database, including SCR and XPSP standard stars.

By comparing BEST stars with USS photometry, we identified spatially dependent systematic errors of about 30–40 mmag in the blue filters (u, J0378, and J0395) and around 10 mmag in other filters. These errors presented a correlation across bands, likely due to the improper handling of stellar metallicity in the SL method and the ATLAS catalog used for the original calibration.

We also discovered position-dependent CCD systematic errors up to 50 mmag, which correlated with the spatial distribution of the difference between USS `APER_6` and USS magnitudes, and anticorrelated with the distribution of FWHM. We developed a linear model to correct these errors based on FWHM and used a second-order polynomial in X and Y to

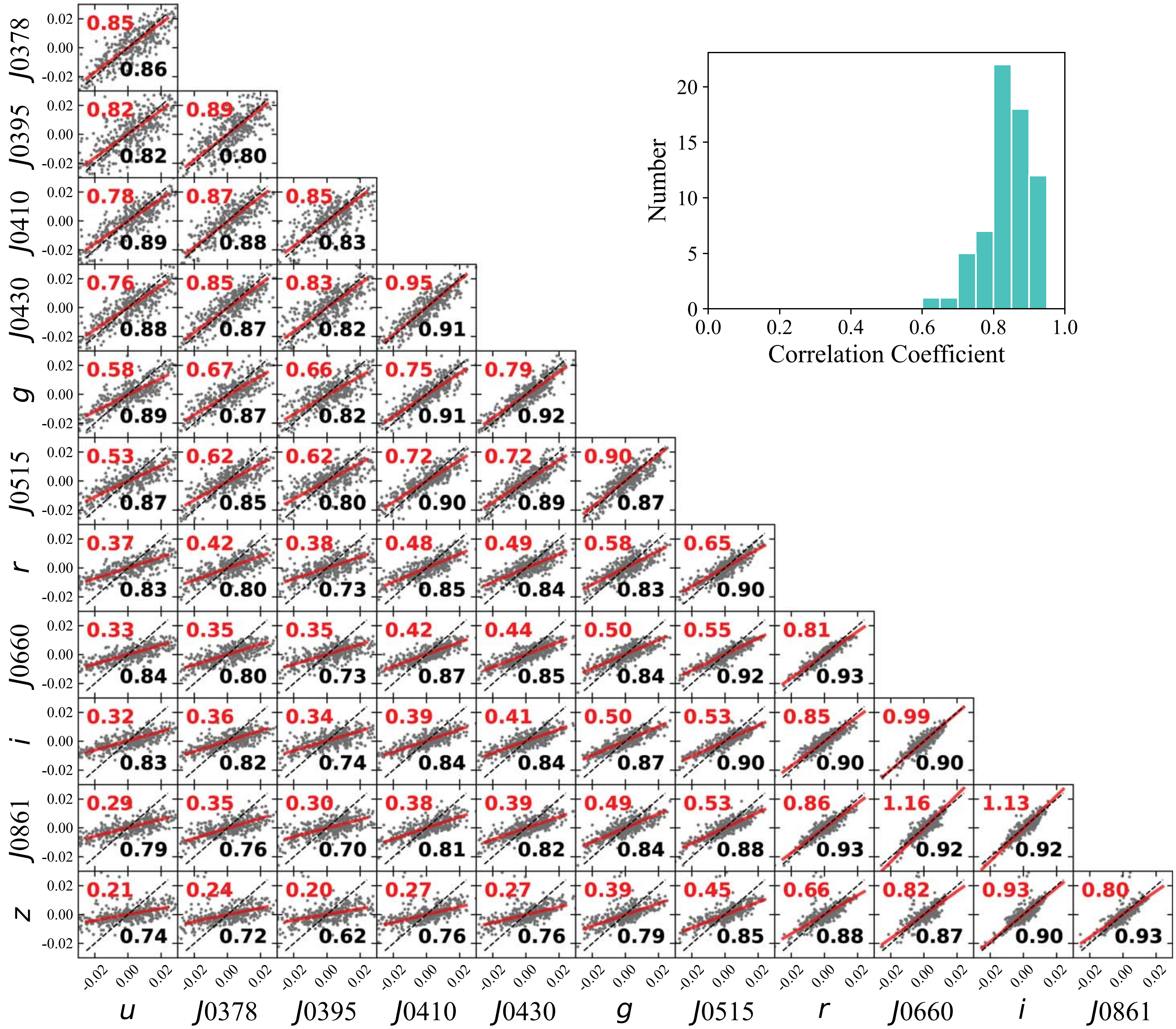

Figure 22. Same as Figure 6, but for the correlation of the 400 values for each of the two bands. For each panel, the correlation coefficients are marked in black in the bottom-right corner. The linear fitting lines are shown as red lines, and the slopes of the lines are marked in red in the top-left corners. The black dashed lines denote $y = x$ in each panel. A histogram of the distribution of the correlation coefficients is shown in the top-right corner.

correct the remaining error. After the corrections, we identified and corrected medium-scale errors up to 50 mmag between large-scale and small-scale flats within the CCD space.

Independent validation using SDSS Stripe 82 and corrected PS1 data presented a fivefold decrease in scatter in the color–color diagrams after recalibration. Validations with LAMOST DR10 and Gaia photometry confirmed a twofold to sixfold improvement. These results highlight the effectiveness of the recalibration and the utility of the BEST database.

We recommend that future USS observations use the BEST database for high-precision photometric calibration, as demonstrated in this study.

Acknowledgments

We sincerely thank the S-PLUS collaboration for providing the USS DR1 photometric data. This work is supported by the NSFC grant Nos. 12403024, 12222301, and 12173007, the National Key Basic R&D Program of China via 2023YFA1608300, the Postdoctoral Fellowship Program of CPSF under grant number GZB20240731, the Young Data Scientist Project of the National Astronomical Data Center, and the China Postdoctoral Science Foundation No. 2023M743447 Y.T. is supported by the International Centre of Supernovae, Yunnan Key Laboratory (Nos. 202302AN360001 and 202302AN36000103). T.C.B. acknowledges partial support from grant PHY 14-30152, Physics Frontier Center/JINA Center for the Evolution of the Elements (JINA-CEE), and from OISE-1927130: The International Research Network for Nuclear Astrophysics (IReNA), awarded by the US National Science Foundation. P.K.H. gratefully acknowledges the Fundação de Amparo à Pesquisa do Estado de São Paulo (FAPESP) for the support grant 2023/14272-4. A.A.-C.

acknowledges financial support from the Severo Ochoa grant CEX2021-001131-S funded by MCIN/AEI/10.13039/501100011033 and the Spanish project PID2023-153123NB-I00 funded by MCIN/AEI. N.G. is supported by the Dezhou University School-level Cultivation Project 2020xjpy06.

The S-PLUS project, including the T80-South robotic telescope and the S-PLUS scientific survey, was founded as a partnership between the Fundação de Amparo à Pesquisa do Estado de São Paulo (FAPESP), the Observatório Nacional (ON), the Federal University of Sergipe (UFS), and the Federal University of Santa Catarina (UFSC), with important financial and practical contributions from other collaborating institutes in Brazil, Chile (Universidad de La Serena), and Spain (Centro de Estudios de Física del Cosmos de Aragón, CEFCA). We further acknowledge financial support from the São Paulo Research Foundation (FAPESP), the Fundação de Amparo à Pesquisa do Estado do RS (FAPERGS), the Brazilian National Research Council (CNPq), the Coordination for the Improvement of Higher Education Personnel (CAPES), the Carlos Chagas Filho Rio de Janeiro State Research Foundation (FAPERJ), and the Brazilian Innovation Agency (FINEP). The authors who are members of the S-PLUS collaboration are grateful for the contributions from CTIO staff in helping in the construction, commissioning, and maintenance of the T80-South telescope and camera. We are also indebted to Rene Laporte and INPE, as well as to Keith Taylor, for their important contributions to the project. From CEFCA, we particularly would like to thank Antonio Marín-Franch for his invaluable contributions in the early phases of the project, David Cristóbal-Hornillos and his team for their help with the installation of the data reduction package jype version 0.9.9, César Íñiguez for providing two-dimensional measurements of the filter transmissions, and all other staff members for their support with various aspects of the project.

This work has made use of data from the European Space Agency (ESA) mission Gaia (https://www.cosmos.esa.int/web/gaia), processed by the Gaia Data Processing and Analysis Consortium (DPAC, https://www.cosmos.esa.int/web/gaia/dpac/consortium). Funding for the DPAC has been provided by national institutions, in particular the institutions participating in the Gaia Multilateral Agreement. Guoshoujing Telescope (the Large Sky Area Multi-object Fiber Spectroscopic Telescope, LAMOST) is a National Major Scientific Project built by the Chinese Academy of Sciences. Funding for the project has been provided by the National Development and Reform Commission. LAMOST is operated and managed by the National Astronomical Observatories, Chinese Academy of Sciences.

Software: Astropy (Astropy Collaboration et al. 2022), Matplotlib (J. D. Hunter 2007), NumPy (C. R. Harris et al. 2020), SciPy (P. Virtanen et al. 2020).

Appendix

This appendix provides the spatial distribution of the magnitude difference between `Aper_3` and `Pstotal`, and the FWHM correlation for each band pair in the `SHORTS-STRIPE82_0090` tile, shown in Figures A1 and A2, respectively. Examples of the spatial variations of the astrometric offsets between Gaia and the USS in the r band are shown in Figure A3.

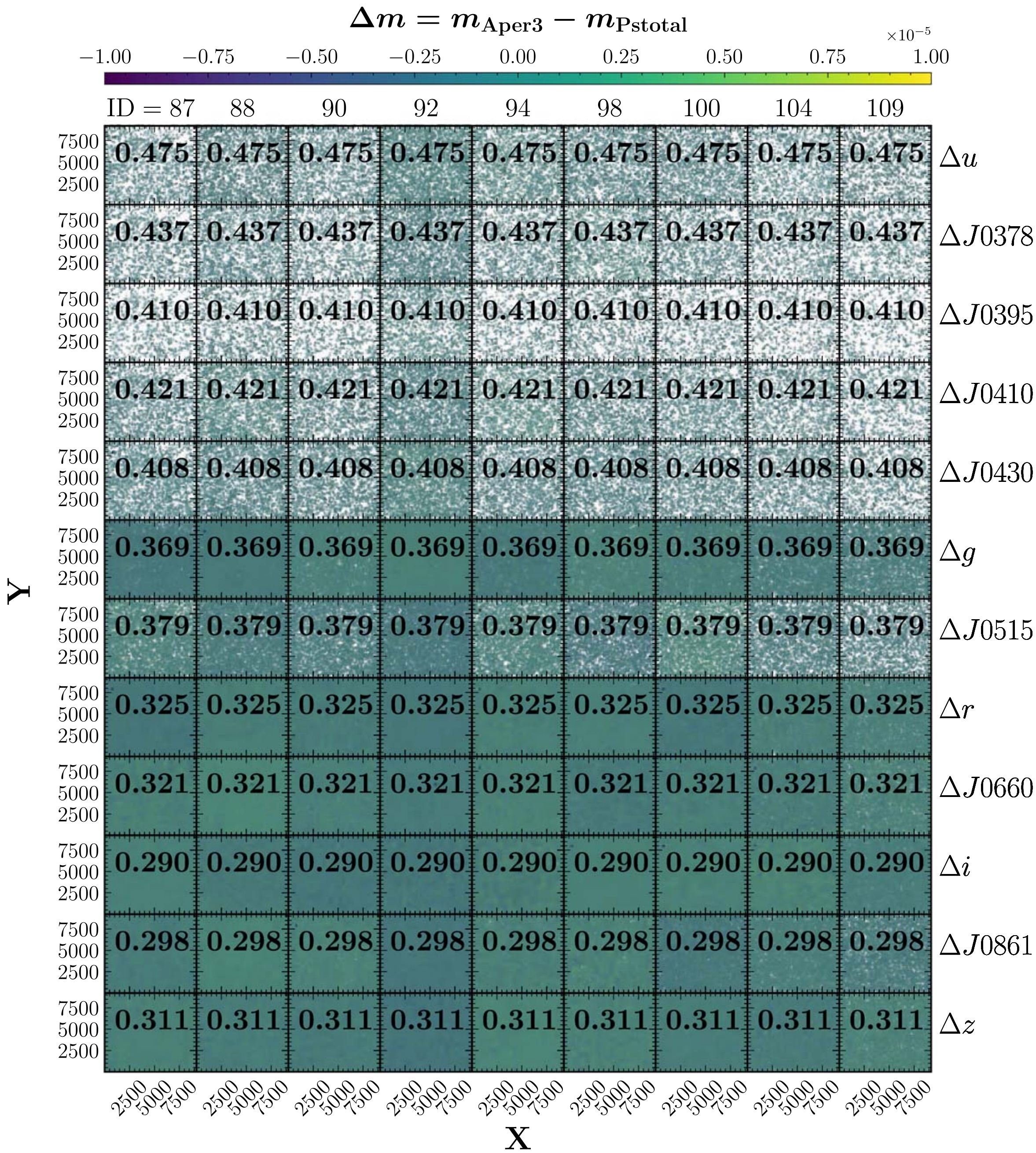

Figure A1. An example showing the CCD spatial distribution of the magnitude difference between `Aper_3` and `Pstotal` for all observed stars within nine tiles. The panels from top to bottom show the results of the *u*, *J*0378, *J*0395, *J*0410, *J*0430, *g*, *J*0515, *r*, *J*0660, *i*, *J*0861, and *z* bands, with band labels on the right and a color bar on top. The selected nine tiles (`SHORTS-STRIPE82_0087`, `SHORTS-STRIPE82_0088`, `SHORTS-STRIPE82_0090`, `SHORTS-STRIPE82_0092`, `SHORTS-STRIPE82_0094`, `SHORTS-STRIPE82_0098`, `SHORTS-STRIPE82_0100`, `SHORTS-STRIPE82_0104`, and `SHORTS-STRIPE82_0109`) are ordered from left to right, with the tile number marked between the first-row panels and the color bar. The median value of the magnitude difference between `Aper_3` and `Pstotal` is indicated in each panel. Note that the color bar ranges from -1×10^{-5} to 1×10^{-5}.

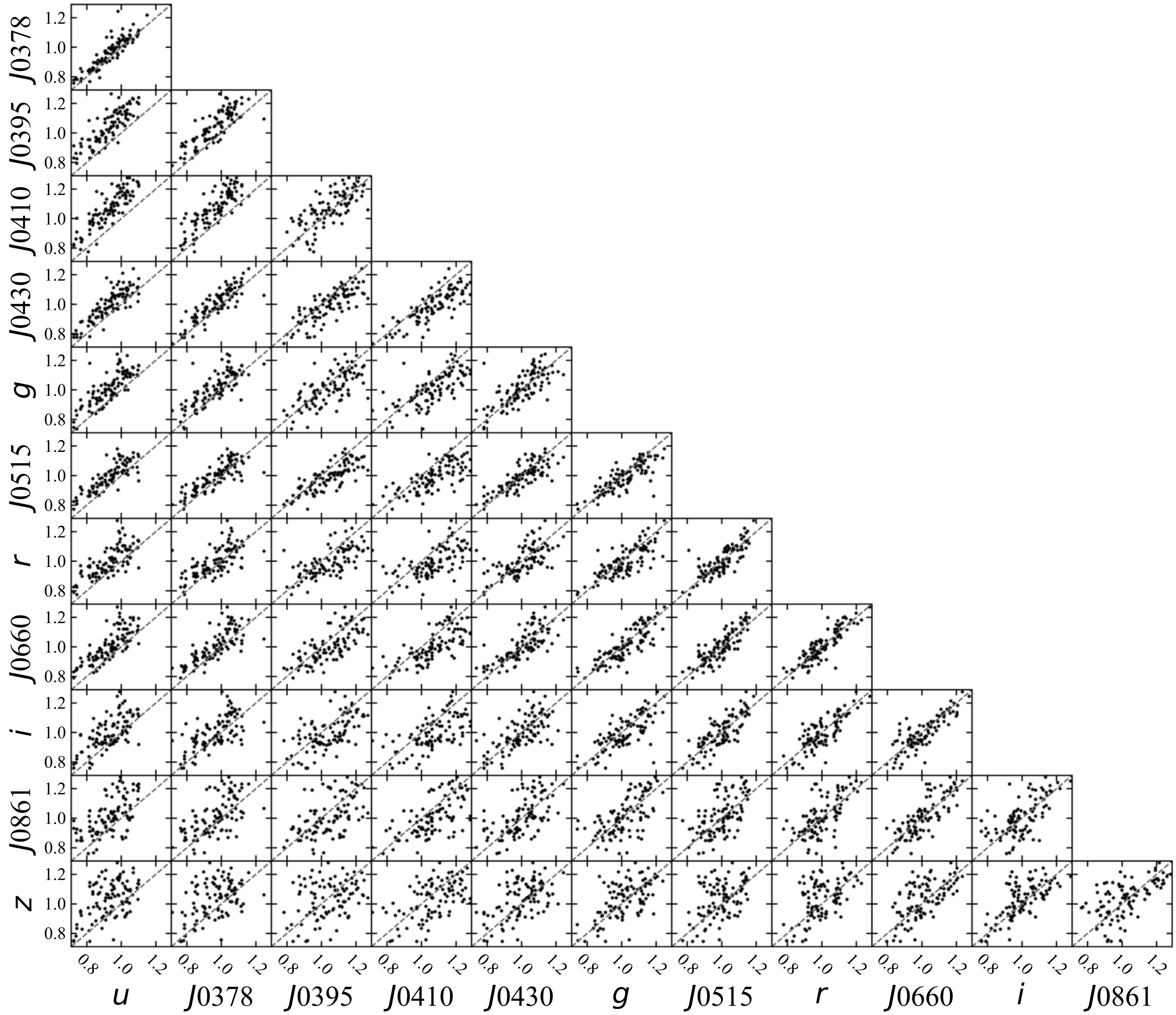

Figure A2. Correlation plots of the normalized FWHM for each of the two bands for `SHORTS-STRIPE82_0090`. The gray dashed lines denote $y = x$ in each panel.

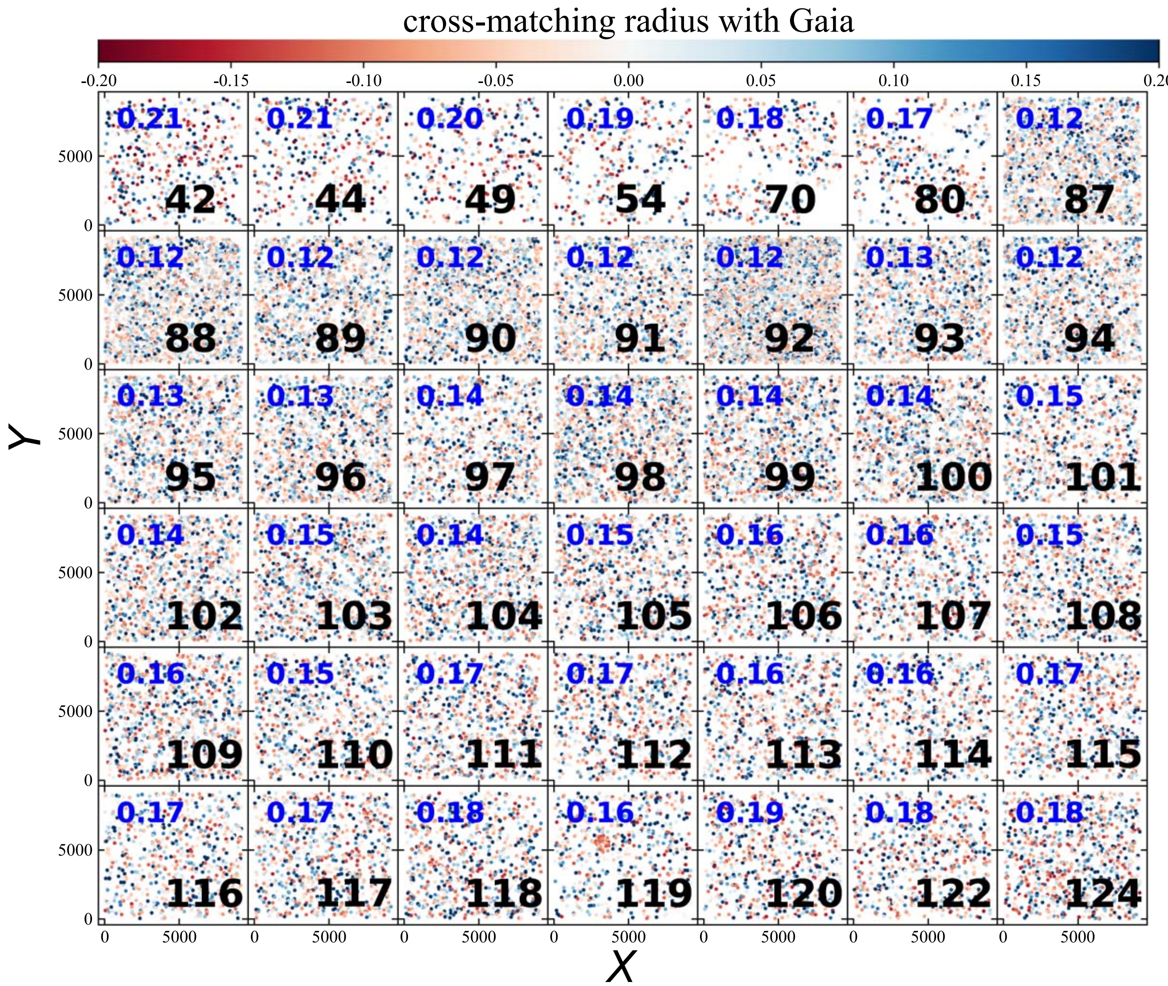

Figure A3. Same as Figure 9, but for the crossmatching radius with Gaia. To clearly display the spatial distribution of the astrometric offsets between the USS and Gaia, we calculated the median value of the astrometric offset for each tile. We then subtracted this median value from all offsets of stars within the tile, and the resulting astrometric offsets are shown in each panel. The `tile_ID` and the median value of the astrometric offset are labeled in the bottom-right and the top-left corner of each panel, respectively.

ORCID iDs

Xiaolu Li https://orcid.org/0009-0007-8288-5656
Kai Xiao https://orcid.org/0000-0001-8424-1079
Yang Huang https://orcid.org/0000-0003-3250-2876
Haibo Yuan https://orcid.org/0000-0003-2471-2363
Yanke Tang https://orcid.org/0000-0003-4207-1694
Timothy C. Beers https://orcid.org/0000-0003-4573-6233
Bowen Huang https://orcid.org/0000-0002-1259-0517
Mingyang Ma https://orcid.org/0009-0003-1069-1482
Pedro K. Humire https://orcid.org/0000-0003-3537-4849
Alvaro Alvarez-Candal https://orcid.org/0000-0002-5045-9675
Federico Sestito https://orcid.org/0000-0002-3182-3574
Ning Gai https://orcid.org/0000-0002-9308-587X
Hongrui Gu https://orcid.org/0009-0007-5610-6495
Zhenzhao Tao https://orcid.org/0000-0002-4683-5500
Lin Yang https://orcid.org/0000-0002-9824-0461
Shuai Xu https://orcid.org/0000-0003-3535-504X

References

Almeida-Fernandes, F., SamPedro, L., Herpich, F. R., et al. 2022, MNRAS, 511, 4590
Astropy Collaboration, Price-Whelan, A. M., Lim, P. L., et al. 2022, ApJ, 935, 167
Benitez, N., Dupke, R., Moles, M., et al. 2014, arXiv:1403.5237
Bertin, E., & Arnouts, S. 1996, A&AS, 117, 393
Carrasco, J. M., Weiler, M., Jordi, C., et al. 2021, A&A, 652, A86
Cenarro, A. J., Moles, M., Cristóbal-Hornillos, D., et al. 2019, A&A, 622, A176
Clem, J. L., & Landolt, A. U. 2013, AJ, 146, 88
Clem, J. L., & Landolt, A. U. 2016, AJ, 152, 91
Cui, X.-Q., Zhao, Y.-H., Chu, Y.-Q., et al. 2012, RAA, 12, 1197
De Angeli, F., Weiler, M., Montegriffo, P., et al. 2023, A&A, 674, A2
Deng, L.-C., Newberg, H. J., Liu, C., et al. 2012, RAA, 12, 735
Fan, Z., Zhao, G., Wang, W., et al. 2023, ApJS, 268, 9
De Silva, G. M., Freeman, K. C., Bland-Hawthorn, J., et al. 2015, MNRAS, 449, 2604
Gaia Collaboration, Brown, A. G. A., Vallenari, A., et al. 2018, A&A, 616, A1
Gaia Collaboration, Brown, A. G. A., Vallenari, A., et al. 2021a, A&A, 649, A1
Gaia Collaboration, Brown, A. G. A., Vallenari, A., et al. 2021b, A&A, 650, C3
Gaia Collaboration, Montegriffo, P., Bellazzini, M., et al. 2023a, A&A, 674, A33
Gaia Collaboration, Vallenari, A., Brown, A. G. A., et al. 2023b, A&A, 674, A1
Harris, C. R., Millman, K. J., van der Walt, S. J., et al. 2020, Natur, 585, 357
Huang, B., Xiao, K., & Yuan, H. 2022, SSPMA, 52, 289503
Huang, B., & Yuan, H. 2022, ApJS, 259, 26
Huang, B., Yuan, H., Xiang, M., et al. 2024, ApJS, 271, 13
Huang, Y., Beers, T. C., Xiao, K., et al. 2024, ApJ, 974, 192
Huang, Y., Yuan, H., Li, C., et al. 2021, ApJ, 907, 68
Hunter, J. D. 2007, CSE, 9, 90
Ivezić, Ž., Kahn, S. M., Tyson, J. A., et al. 2019, ApJ, 873, 111

Ivezić, Ž., Smith, J. A., Miknaitis, G., et al. 2007, AJ, 134, 973
Liu, J., Soria, R., Wu, X.-F., et al. 2021, AnABC, 93, 20200628
Liu, X.-W., Yuan, H.-B., Huo, Z.-Y., et al. 2014, in IAU Symp. 298, Setting the Scene for Gaia and LAMOST, ed. S. Feltzing et al. (Cambridge: Cambridge Univ. Press), 310
López-Sanjuan, C., Vázquez Ramió, H., Xiao, K., et al. 2024, A&A, 683, A29
Montegriffo, P., De Angeli, F., Andrae, R., et al. 2023, A&A, 674, A3
Niu, Z., Yuan, H., & Liu, J. 2021a, ApJ, 909, 48
Niu, Z., Yuan, H., & Liu, J. 2021b, ApJL, 908, L14
Perottoni, H. D., Placco, V. M., Almeida-Fernandes, F., et al. 2024, A&A, 691, A138
Mendes de Oliveira, C., Ribeiro, T., Schoenell, W., et al. 2019, MNRAS, 489, 241
Schlegel, D. J., Finkbeiner, D. P., & Davis, M. 1998, ApJ, 500, 525
Stubbs, C. W., & Tonry, J. L. 2006, ApJ, 646, 1436
Sun, Y., Yuan, H., & Chen, B. 2022, ApJS, 260, 17
Tonry, J. L., Denneau, L., Flewelling, H., et al. 2018, ApJ, 867, 105
Tonry, J. L., Stubbs, C. W., Lykke, K. R., et al. 2012, ApJ, 750, 99
Virtanen, P., Gommers, R., Oliphant, T. E., et al. 2020, NatMe, 17, 261
Wolf, C., Onken, C. A., Luvaul, L. C., et al. 2018, PASA, 35, e010
Xiao, K., Huang, B., Huang, Y., et al. 2024a, ApJL, 968, L24
Xiao, K., Huang, Y., Yuan, H., et al. 2024b, ApJS, 271, 41
Xiao, K., & Yuan, H. 2022, AJ, 163, 185
Xiao, K., Yuan, H., Huang, B., et al. 2023a, ChSBu, 68, 2790
Xiao, K., Yuan, H., Huang, B., et al. 2023b, ApJS, 268, 53
Xiao, K., Yuan, H., López-Sanjuan, C., et al. 2023c, ApJS, 269, 58
Yang, L., Yuan, H., Zhang, R., et al. 2021, ApJL, 908, L24
York, D. G., Adelman, J., Anderson, J. E., et al. 2000, AJ, 120, 1579
Yuan, H., Liu, X., Xiang, M., et al. 2015, ApJ, 799, 133
Yuan, H. B., Liu, X. W., & Xiang, M. S. 2013, MNRAS, 430, 2188
Zhan, H. 2018, 42nd COSPAR Scientific Assembly, 42 E1.16-4-18
Zhang, R., & Yuan, H. 2020, ApJL, 905, L20
Zhang, R., & Yuan, H. 2023, ApJS, 264, 14
Zhao, G., Zhao, Y.-H., Chu, Y.-Q., et al. 2012, RAA, 12, 723
Zheng, J., Zhao, G., Wang, W., et al. 2018, RAA, 18, 147
Zheng, J., Zhao, G., Wang, W., et al. 2019, RAA, 19, 3